RSC Advances

PAPER

View Article Online
View Journal | View Issue

Cite this: *RSC Adv.*, 2026, **16**, 23783

Development and application of a shrimp shell waste/$FeCl_2$-$FeCl_3$ composite as an efficient bioadsorbent for dye removal from textile effluents

Hilana Saker,[a] Chahrazed Djilani,[ab] Nada Hamrouche,[cd] Pierre Magri,[e] Rachida Zaghdoudi,[bf] Samar Hadroug,[g] Ahmed Hichem Hamzaoui,[h] Leila El-Bassi[g] and Djihane Slimane Ben Ali *[i]

This study investigates the preparation and characterization of a bio-based adsorbent derived from shrimp shells, chemically modified with $FeCl_2$ and $FeCl_3$, for the efficient removal of methylene blue (MB) from aqueous solutions. This research aims to transform seafood waste into a high-value composite material for wastewater treatment. Structural and morphological evaluation (XRD, BET, SEM/EDX) confirmed the successful integration of iron oxides, resulting in increased surface roughness and the presence of iron-rich active sites. FTIR analysis identified amine and hydroxyl groups as the primary functional groups responsible for MB binding. Adsorption effects yielded optimal conditions: adsorbent mass of 0.050 g, initial MB concentration of 150 mg L^{-1}, temperature of 25 °C, and solution pH of 12, with a maximum monolayer adsorption capacity of 114.47 mg g^{-1} according to the Langmuir isotherm model. The Elovich model, suggested adsorption on energetically heterogeneous surfaces, while equilibrium data follow the Dubinin–Radushkevich isotherm, indicating a predominantly physical adsorption, best described kinetic data. Thermodynamic analysis further revealed that the process is spontaneous and exothermic. Finally, process optimization using a Box–Behnken design (BBD) under response surface methodology showed high model predictability, establishing this composite as a cost-effective and eco-friendly solution for the remediation of dye-contaminated effluents.

Received 16th February 2026
Accepted 29th April 2026

DOI: 10.1039/d6ra01393g

rsc.li/rsc-advances

1. Introduction

The global freshwater supply represents less than 1% of the Earth's total water volume.[1,2] Despite its vital importance, the quality of available water continues to deteriorate, often irreversibly.[3] This scarcity is exacerbated by the rapid expansion of industrial activities, particularly in the textile, paper, and plastic sectors. These industries consume vast quantities of water and discharge effluents containing synthetic dyes, with an estimated global production of 800 000 tons per year. Once released into the environment, these dyes contaminate groundwater and surface water, posing significant risks due to their complex molecular structures, which make them highly stable and resistant to biodegradation.[4–6]

Among these pollutants, methylene blue (MB) is a prominent cationic dye widely used in the pharmaceutical and textile industries.[7] Despite its moderate toxicity, its presence in water bodies obstructs light penetration, disrupts aquatic ecosystems, and poses health risks to humans.[8,9] Consequently, developing effective treatment methods for dye-laden effluents is a critical priority.

Numerous physical, chemical, and biological methods, including flocculation,[10] membrane filtration,[11] ozonation,[12] and photo-degradation,[13,14] have been explored for dye removal, yet they often suffer from high operational costs, incomplete efficiency, or the regeneration of toxic secondary pollutants.[15,16] In contrast, adsorption has emerged as one of the most promising and widely applied methods due to its simplicity, high efficiency, economic feasibility, and ability to remove even low concentrations of contaminants.[17–19] In recent years, increasing attention has focused on developing low-cost, environmentally friendly adsorbents derived from natural or waste materials.

[a]*Faculty of Technologie, University of 20 Août 1955, El Hadaiek Road, B. O. 26, 21000 Skikda, Algeria. E-mail: hi.saker@univ-skikda.dz*
[b]*Laboratory LRPCSI, University of 20 Août1955, El Hadaiek Road, B. O. 26, 21000 Skikda, Algeria*
[c]*Department of Process Engineering, Faculty of Technology, University of 20 Août1955, El Hadaiek Road, B. O. 26, 21000 Skikda, Algeria*
[d]*Laboratory of Catalysis, Bioprocesses and Environment (LCBE), University 20 August 1955, Skikda 21000, Algeria*
[e]*LCP-A2MC, University of Lorraine, ICPM, 1 bd Arago, 57078 Metz, France*
[f]*Faculty of Science, University of 20 Août1955, El Hadaiek Road, B. O. 26, 21000 Skikda, Algeria*
[g]*Centre National de Recherches en Sciences des Matériaux, Soliman, Tunisia*
[h]*Wastewaters and Environment Laboratory, Water Research and Technologies Center (CERTE), Soliman, Tunisia*
[i]*Department of Petrochemical, Faculty of Technology, University of 20 Août1955, El Hadaiek Road, B. O. 26, 21000 Skikda, Algeria*

However, textile industrial effluents are complex matrices containing not only dyes like Methylene Blue but also heavy metals (Cu, Zn, or Pb), bleaching agents, and various salts. These components can significantly alter pH and salinity, potentially competing with dye molecules for adsorption sites. This study focuses on a mono-component aqueous system as a preliminary evaluation of the adsorbent's fundamental performance.[20]

In this context, the valorization of seafood waste,[21,22] specifically the shells of the red shrimp *Aristeus antennatus* (Risso, 1816),[23,24] presents a promising solution. These shells are rich in chitin, proteins, and calcium carbonates, which provide functional groups such as hydroxyl (–OH), amino ($-NH_2$), amide (–CONH–), and carbonyl (C=O).[25,26] These groups enable interactions with methylene blue (MB) through various mechanisms, including electrostatic attraction, hydrogen bonding, π–π interactions, and electron donor–acceptor interactions, thereby facilitating effective dye binding on the biosorbent surface.[27,28] The synergistic effect of these physicochemical interactions accounts for the high adsorption capacity and efficiency of shrimp shells in sustainable dye removal. Consequently, employing shrimp shells as a biosorbent combines superior adsorption performance, biomass waste valorization, and operational simplicity, offering a cost-effective and environmentally friendly approach to treating colored industrial effluents.

The novelty of this work lies in the chemical modification of raw shrimp shells (SSW) using a specific binary mixture of $FeCl_2$ and $FeCl_3$. Unlike standard single-salt treatments, the combined use of $FeCl_2$/$FeCl_3$ is designed to significantly enhance the surface properties, porosity, and chemical affinity of the waste shells for dye molecules, thereby maximizing adsorption performance. Similar observations were reported in previous studies.[29,30]

This study focuses on the preparation and comprehensive characterization of SSW/$FeCl_2$-$FeCl_3$ adsorbents. The physicochemical properties were analyzed using Fourier Transform Infrared spectroscopy (FTIR), Scanning Electron Microscopy coupled with Energy Dispersive X-ray analysis (SEM/EDX), X-ray Diffraction (XRD), Brunauer–Emmett–Teller (BET) surface area analysis, laser diffraction particle size and point of zero charge analysis. Batch adsorption experiments were conducted to evaluate the influence of adsorbent dosage, contact time, initial dye concentration and pH solution. To maximize the removal efficiency, the process parameters were optimized using response surface methodology (RSM) based on a Box–Behnken Design (BBD). This statistical approach was employed to investigate the interactive effects of the variables and to determine the optimal conditions for the adsorption process. Furthermore, adsorption kinetics, equilibrium isotherms, and thermodynamic parameters were investigated to elucidate the underlying mechanisms and temperature dependence.

Ultimately, this research aims to demonstrate the feasibility of SSW/$FeCl_2$-$FeCl_3$ as a high-performance, sustainable, and low-cost biosorbent, promoting the transition toward a circular economy through the valorization of bio-waste.

2. Materials and methods

2.1. Preparation of shrimp shell waste (SSW)

Shrimp shell waste was collected from various restaurants in the city of Skikda, Algeria. This biomass primarily comprised the heads, shells, and appendages remaining after the peeling process. To remove impurities and dirt, the raw material was thoroughly washed with cold water. The cleaned shells were subsequently dried using a combination of solar energy and oven-drying until a constant weight was achieved. Once completely dehydrated, the shells were ground into a fine powder using an electric grinder and passed through a fine-mesh sieve to ensure particle size uniformity. The resulting shrimp shell powder (SSP) was stored in airtight containers and maintained in a cool, dry environment for subsequent use.

2.2. Modification of shrimp shell

The modification of shrimp shells was performed using a co-precipitation method. 5 g of SSW were introduced into an aqueous solution containing 2.40 g of $FeCl_2$ and 1.08 g of $FeCl_3$ (molar ratio Fe^{2+}/Fe^{3+} 3 : 1). The suspension was stirred at 65 °C to promote the interaction between iron ions and the functional groups present on the SSW surface. Subsequently, 5 g of NaOH were added to the mixture to increase the pH and induce the co-precipitation of iron hydroxides onto the SSW surface. The resulting suspension was stirred for one hour to ensure homogeneous deposition of iron species. Finally, the mixture was washed several times with distilled water and dried at 100 °C to yield the final adsorbent material.[31]

2.3. Characterization of adsorbent

Fourier transform infrared spectroscopy (ATR-FTIR, Vertex 80v, Bruker) in reflection mode was employed to identify the functional groups present on the surface of the two materials (SSW and SSW/$FeCl_2$-$FeCl_3$) before and after methylene blue (MB) adsorption. The crystalline structures of the materials were determined using X-ray diffraction (XRD) with a PANalytical Empyrean instrument. Scanning electron microscopy coupled with energy dispersive X-ray spectrometry (SEM/EDX) was performed to examine the surface morphology and elemental composition of SSW, SSW/$FeCl_2$-$FeCl_3$, and SSW/$FeCl_2$-$FeCl_3$-MB adsorbents. The specific surface area of the two materials was determined using the Brunauer–Emmett–Teller (BET) method with an ANSAP 2020 plus instrument.

The particle size distributions of raw and modified shrimp shell, and shrimp shell after adsorption were determined using a Microtrac S3500 laser diffraction analyzer. To evaluate the width of these distributions for the materials (SSW, SSW/$FeCl_2$-$FeCl_3$, and SSW/$FeCl_2$-$FeCl_3$-MB), the SPAN index was calculated using the following eqn (1):[32]

$$\mathrm{SPAN} = \frac{D_{90} - D_{10}}{D_{50}} \quad (1)$$

In this context, the characteristic diameters D_{10}, D_{50}, and D_{90} represent the particle sizes below which 10%, 50%, and 90% of the cumulative volume distribution are found, respectively.[33]

A low SPAN value indicates a homogeneous and narrow distribution, whereas higher values represent polydispersity.[34]

To determine the point of zero charge (pH_{pzc}) of the studied material, 0.2 g of SSW/$FeCl_2$-$FeCl_3$ was added to 50 ml of a 0.1 M of NaCl solution. The initial pH (pH_i) of the samples was varied across a range of 2 to 12 and adjusted using 0.1 M HCl or NaOH. The resulting suspensions were stirred for 24 h at 400 rpm to reach equilibrium.

Following the equilibrium period, the final pH (pH_f) of each solution was measured. The pH_{pzc} is determined by plotting the change in pH ($\Delta pH = pH_f - pH_i$) against the initial pH (pH_i); the point where the curve intersects the x-axis ($\Delta pH = 0$) represents the pH_{pzc}.

2.4. Adsorption experiments

Batch adsorption experiments were conducted to evaluate the adsorption capacity of SSW/$FeCl_2$-$FeCl_3$ for methylene blue (MB) in a fixed volume of 50 ml. Diluted MB solutions were prepared with initial concentrations ranging from 10 to 150 mg L^{-1} using a 1 g L^{-1} stock solution (initial pH ~6.8). Adsorbent dose was first optimized at 0.025, 0.05, 0.10, 0.15, and 0.2 g under fixed conditions: 25 °C, 90 min contact time, 100 mg L^{-1} initial MB concentration, and 400 rpm agitation. The optimal dose of 0.05 g was then used for all subsequent experiments (50 ml volume). For each, 0.05 g of adsorbent was added to an Erlenmeyer flask containing the MB solution, sealed with Parafilm, and stirred for 90 min at 25 °C and 400 rpm using a thermostatic stirrer.

The influence of operating parameters was systematically investigated under optimized conditions (0.050 g dose, 50 ml volume, 400 rpm), with all tests performed in triplicate ($n = 3$; error bars in figures represent mean ± SD). Contact time was varied from 1 to 90 min at pH ~6.8, 100 mg L^{-1} initial MB, and 25 °C (data used to fit kinetic models); initial MB concentration from 10 to 150 mg L^{-1} at pH ~6.8, 25 °C, and 90 min (data used to fit isotherm models); pH from 2 to 12 at 100 mg L^{-1} initial MB, 25 °C, and 90 min; and temperature at 25, 30, 40, and 50 °C at pH ~6.8, 100 mg L^{-1} initial MB, and 90 min. Upon completion of each adsorption test, the suspensions were centrifuged. The resulting supernatant solution was then analyzed using a UV-Vis spectrophotometer (PerkinElmer Lambda 25) to determine the remaining concentration of methylene blue.

The amount of MB adsorbed by SSW/$FeCl_2$-$FeCl_3$ adsorbent (q_e in mg g^{-1}) and the removal efficiency (% removal) were calculated using the following equations:[35–37]

$$q_e = \frac{C_0 - C_e}{m} \times V \quad (2)$$

$$\%\ \text{removal} = \frac{C_0 - C_e}{C_0} \times 100 \quad (3)$$

where: C_0 (mg L^{-1}) is the initial concentration of MB, C_e (mg L^{-1}) is the concentration of MB in the equilibrium state, m (g) is mass of SSW/$FeCl_2$-$FeCl_3$ and V (L) is the volume of MB solution (containing SSW/$FeCl_2$-$FeCl_3$).

2.5. Box–Behnken design based RSM

Response surface methodology (RSM) is a statistical approach used to explore and understand how several input variables simultaneously influence one or more output responses. By applying experimental designs, such as Central Composite (CCD) or Box–Behnken (BBD) designs, this method enables efficient data collection through fewer experimental runs, thereby optimizing time and resource usage.[38] In this study, a Box–Behnken design was employed to investigate the influence of key factors specifically pH, temperature, and initial dye concentration on the decolorization process. Eqn (4) was used to calculate the required number of experiments (N) for the BBD model:

$$N = 2K(K - 1) + C \quad (4)$$

where K represents the number of independent variables and C represents the number of center point replicates.[39] Based on these parameters, a total of 17 experiments were determined, as shown in Table S1. These experimental runs were generated using three levels for each variable: low (−1), medium (0), and high (1), as detailed in Table S2. In RSM, a full quadratic equation is typically employed. The second-order model is expressed as shown in eqn (5):[40]

$$Y = \beta_0 + \sum_{i=0}^{n} \beta_i X_i + \sum_{i=0}^{n} \beta_{ii} X_i^2 + \sum_{i=1}^{n-1} \sum_{j=1+1}^{n} \beta_{ij} X_i X_j \quad (5)$$

In this model, Y represents the predicted response (the removal of MB using SSW/$FeCl_2$-$FeCl_3$), and X denotes the independent variables. The coefficients β_0, β_j, β_{jj}, and β_{ij} correspond to the intercept, linear effects, quadratic effects, and interaction effects, respectively. The variable n represents the number of coded input variables.[41] The regression parameters, including the correlation coefficient (R^2), adjusted R^2, F-value (Fisher's ratio), and p-value (probability value), were determined using Design-Expert version 13 software through analysis of variance (ANOVA) to evaluate the accuracy and suitability of the predictive model. Based on a 95% confidence level, the significance of the independent variables on the MB adsorption process was then examined.[39,42]

2.6. Adsorption kinetic

Adsorption kinetics is crucial for understanding the rate and mechanism of solute uptake onto an adsorbent surface. Kinetic modeling provides insights into whether the adsorption process is governed by chemical reactions, diffusion, or mass transfer phenomena.[43] In this study, non-linear kinetic models namely the pseudo-first-order (PFO), pseudo-second-order (PSO), Elovich and intra-particle diffusion (IPD) models were applied to the experimental data to elucidate the adsorption mechanism of methylene blue (MB) onto the treated SSW/$FeCl_2$-$FeCl_3$ composite.

2.6.1. Pseudo-first-order model (PFO). The PFO model, proposed by Lagergren (1898), assumes that rate of adsorption is proportional to the number unoccupied sites on the adsorbent surface. Its non-linear form is expressed as:[44,45]

$$q_t = q_e(1 - e^{k_1 t}) \quad (6)$$

where: q_t (mg g^{-1}) and q_e (mg g^{-1}) are the adsorption capacities at time t and at equilibrium, respectively, and k_1 (min^{-1}) is the rate constant for the PFO model. This model is mainly applicable when physical adsorption predominates during the process.

2.6.2. Pseudo-second-order (PSO). The PSO model (Ho and McKay, 1999) assumes that chemisorption, involving valence forces through sharing or exchange of electrons between adsorbent and adsorbate controls the adsorption rate. The non-linear form of this model is:[44,46]

$$q_t = \frac{q_e k_2 t}{1 + k_2 q_e t} \quad (7)$$

where: k_2 (g mg^{-1} min^{-1}) is the PSO rate constant. This model often fits well for systems where chemical interactions dominate the adsorption process.

2.6.3. Intra-particle diffusion (IPD) model. The IPD model, proposed by Weber and Morris (1963), helps to identify the diffusion mechanism controlling the adsorption process. The non-linear and linear forms of this model is given by:[47,48]

$$q_t = K_{id} t^{1/2} + C \quad (8)$$

where: K_{id} (mg mg^{-1} min$^{-1/2}$) is the intra-particle diffusion rate constant and C (mg g^{-1}) is the intercept related to the boundary layer thickness. Analysis of the IPD model helps to determine whether the adsorption rate is governed primarily by diffusion within the pores or by film transport resistance, providing deeper understanding of the mechanism of the overall adsorption process.

2.6.4. Elovich model. The Elovich model is widely used to describe heterogeneous adsorption surfaces. It assumes that the number of active sites increases exponentially with adsorption, implying decrease in adsorption rate as surface coverage increases. The non-linear form is:[49,50]

$$q_t = \frac{1}{\beta}\ln(1 + \alpha\beta t) \quad (9)$$

where: α (mg g^{-1} min^{-1}) is the initial adsorption rate and β (g mg^{-1}) is desorption constant related to the extent of surface coverage and activation energy for chemisorption.

2.7. Adsorption isotherms

To characterize the capacity of this material for MB fixation and to better understand the adsorption mechanism, the experimental data were analyzed using the non-linear equations of Langmuir (eqn (10)), Freundlich (eqn (12)) and Temkin (eqn (13)):[51–53]

$$q_e = \frac{q_m K_L C_e}{1 + K_L C_e} \quad (10)$$

The favorability of the adsorption process was evaluated using the dimentionless separation factor R_L, calculated according to eqn (11), with the following criteria: $R_L > 1$ (unfavorable adsorption), $R_L = 1$ (linear adsorption), $0 < R_L < 1$ (favorable adsorption), $R_L = 0$ (irreversible adsorption).[54,55]

$$R_L = \frac{1}{1 + K_L C_0} \quad (11)$$

$$q_e = K_F C_e^{1/n} \quad (12)$$

$$q_e = B_T \ln(K_T C_e) \quad (13)$$

where: q_e (mg g^{-1}) is the amount of dye adsorbed at equilibrium, q_m (mg g^{-1}) is the maximum monolayer adsorption capacity, C_e (mg L^{-1}) is the equilibrium concentration of MB, K_L (L mg^{-1}) is the Langmuir constant related to adsorption energy, K_F (mg g^{-1})(L mg^{-1})$^{1/n}$ is the Freundlich constant indicating adsorption capacity, n represents adsorption intensity, B_T (J mol^{-1}) is the constant related to the heat of adsorption, and K_T (L mg^{-1}) is the Temkin equilibrium constant.

The Dubinin–Radushkevich (D–R) isotherm is expressed in its linear form as:

$$\ln q_e = \ln q_{mDR} - K_{DR}\varepsilon^2 \quad (14)$$

where q_e (mg g^{-1}) is the amount of adsorbate adsorbed per unit mass of adsorbent at equilibrium, q_{mDR} (mg g^{-1}) is the theoretical D–R monolayer saturation capacity, K_{DR} (mol^2 kJ^{-2}) is the D–R isotherm constant, and ε is the Polanyi potential given by $\varepsilon = RT\ln\left(1 + \frac{1}{C_e}\right)$. Here, R (8.314 J mol^{-1} K^{-1}) is the universal gas constant, T (K) is the absolute temperature, and C_e (mg L^{-1}) is the equilibrium concentration of the adsorbate.

The mean free energy of adsorption per mole adsorbate (E, kJ mol^{-1}) is calculated as:[56–58]

$$E = \frac{1}{\sqrt{2K_{DR}}} \quad (15)$$

The value of E provides insight into the adsorption mechanism:

If $E < 8$ kJ mol^{-1}, the adsorption is physical (physisorption).

If $E > 8$ kJ mol^{-1}, the adsorption is chemical (chemisorption).

3. Resultats and discussion

3.1. Adsorbent characterization

FTIR analysis of SSW, SSW/$FeCl_2$-$FeCl_3$, and SSW/$FeCl_2$-$FeCl_3$-MB materials were performed in the spectral range of 4000–400 cm^{-1} to identify the functional groups involved in methylene blue (MB) adsorption and to clarify the interaction mechanism between the dye and the adsorbent surface. As shown in Fig. 1, the FTIR spectrum of SSW exhibits several characteristic functional groups of shrimp shell biomass. The broad band centered around 3266.15 cm^{-1} corresponds to the stretching vibrations of –OH and N–H groups,[59,60] while the peak near 2925.51 cm^{-1} is attributed to C–H stretching. The signal observed at approximately 1630.16 cm^{-1} is assigned to the C=O vibration of amide I.[59] The bands around 1025.54 and 695.71 cm^{-1} are related to C–N and N–H bending vibrations,

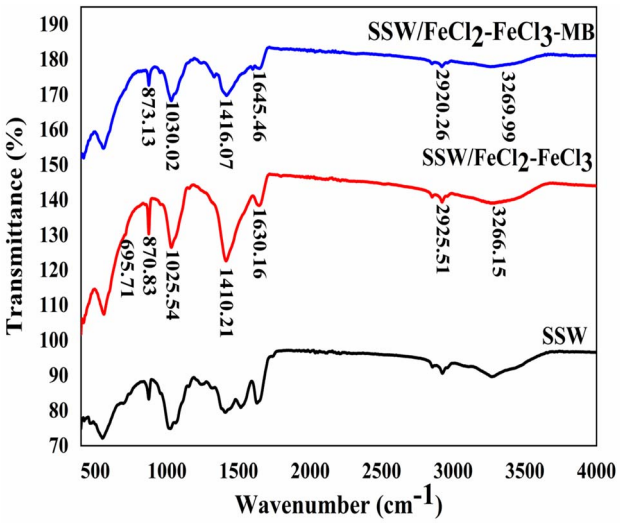

Fig. 1 FTIR spectra of SSW and SSW/$FeCl_2$-$FeCl_3$ before and after adsorption.

respectively. Additionally, peaks located at 1410.21 and 870.83 cm^{-1} confirm the presence of carbonate ions (CO_3^{-2}), typical of aragonite ($CaCO_3$), which are generally detected within the ranges 1490–1410 cm^{-1} and 880–860 cm^{-1}.[61] Following the modification of SSW with the $FeCl_2$–$FeCl_3$ couple, a noticeable increase in the intensity of several IR bands was observed, indicating the formation of new chemical interactions, likely due to the complexation of the support's functional groups with Fe^{2+} and Fe^{3+} ions. These spectral changes reflect a structural reorganization that enhances the density of available active sites.

After the adsorption of methylene blue (MB), significant modifications in the FTIR spectra of SSW/$FeCl_2$-$FeCl_3$ were observed, confirming the successful fixation of the dye onto the adsorbent surface (Table 1 and Fig. 1). Specifically, the disappearance of the N–H bending vibration at 695.71 cm^{-1} suggests that these groups are directly involved in the binding process, likely through hydrogen bonding with the MB molecules. Furthermore, the decrease in intensity and the shift of the –OH and –NH stretching bands (from 3266.15 to 3269.99 cm^{-1}) and the C=O amide I band (from 1630.16 to 1645.46 cm^{-1}) indicate that the lone pairs of electrons on the oxygen and nitrogen atoms of the adsorbent are interacting with the cationic structure of the MB dye. Additionally, the appearance of slight modifications in the 1030 cm^{-1} region (C–N bending) reflects the presence of the aromatic rings and amine groups inherent to the methylene blue structure. These spectral changes-shifts, intensity reductions, and disappearances-collectively demonstrate that the adsorption mechanism is driven by a combination of electrostatic attractions between the cationic dye and the negatively charged sites of the modified shrimp shells, as well as complexation with the iron ions (Fe^{2+}/Fe^{3+}) present on the surface.[62,63]

Table 1 The prominent peaks of SSW/$FeCl_2$-$FeCl_3$ before and after adsorption

Functional groups	Before adsorption (cm^{-1})	After adsorption (cm^{-1})
OH–NH stretching	3266.15	3269.99
C–H stretching	2925.51	2920.26
C=O stretching in amide I	1630.16	1645.46
CO_3O^{2-} (calcite)	1410.21	1416.07
C–N bending	1025.54	1030.02
CO_3O^{2-} (calcite)/C–H stretching	870.83	873.13
N–H bending	695.71	—

The X-ray diffraction (XRD) patterns demonstrate a significant structural transformation of raw shrimp shells (SSW) following modification with a $FeCl_2$/$FeCl_3$ solution. The initial diffractogram of the raw shrimp shell (Fig. 2) exhibits characteristic sharp peaks at 2θ values of approximately 9°, 19°, and 26–30°, reflecting a semi-crystalline biological structure composed of an α-chitin organic matrix and mineral components like calcium carbonate ($CaCO_3$). Specifically, the well-ordered crystalline peaks at 9.3° (020 plane) and 19.2° (110 plane) serve as characteristics for α-chitin, while the intense peak near 29.4° corresponds to the (104) plane of calcite.[64–66] In contrast, the second diffractogram (Fig. 2) reveals radical changes in the material's surface and internal structure. A noticeable broadening of peaks and a reduction in intensity suggest a loss of crystallinity, likely due to partial demineralization or disruption of chitin chains by the iron treatment, leading to a more amorphous (disordered) state. Furthermore, the emergence of new, broad humps or peaks at approximately 35.5°, 43°, and 62° indicates the successful functionalization of the shrimp shell through the formation of iron oxide or hydroxide phases, specifically magnetite (Fe_3O_4) or maghemite (γ-Fe_2O_3) nanoparticles, which are essential for applications such as adsorption or catalysis.[67]

SEM micrographs of the raw SSW material (Fig. 3) reveal a compact, heterogeneous, and low-porosity structure composed of irregular fragments and fibrils characteristic of the mineral-organic matrix of shrimp shells, as generally observed

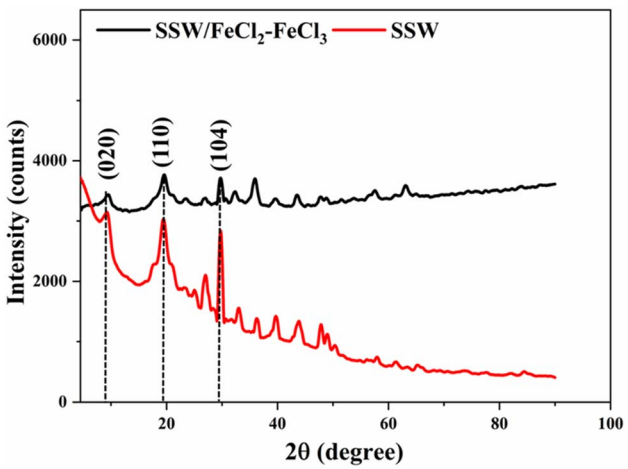

Fig. 2 X-ray diffraction patterns of SSW and SSW/$FeCl_2$-$FeCl_3$.

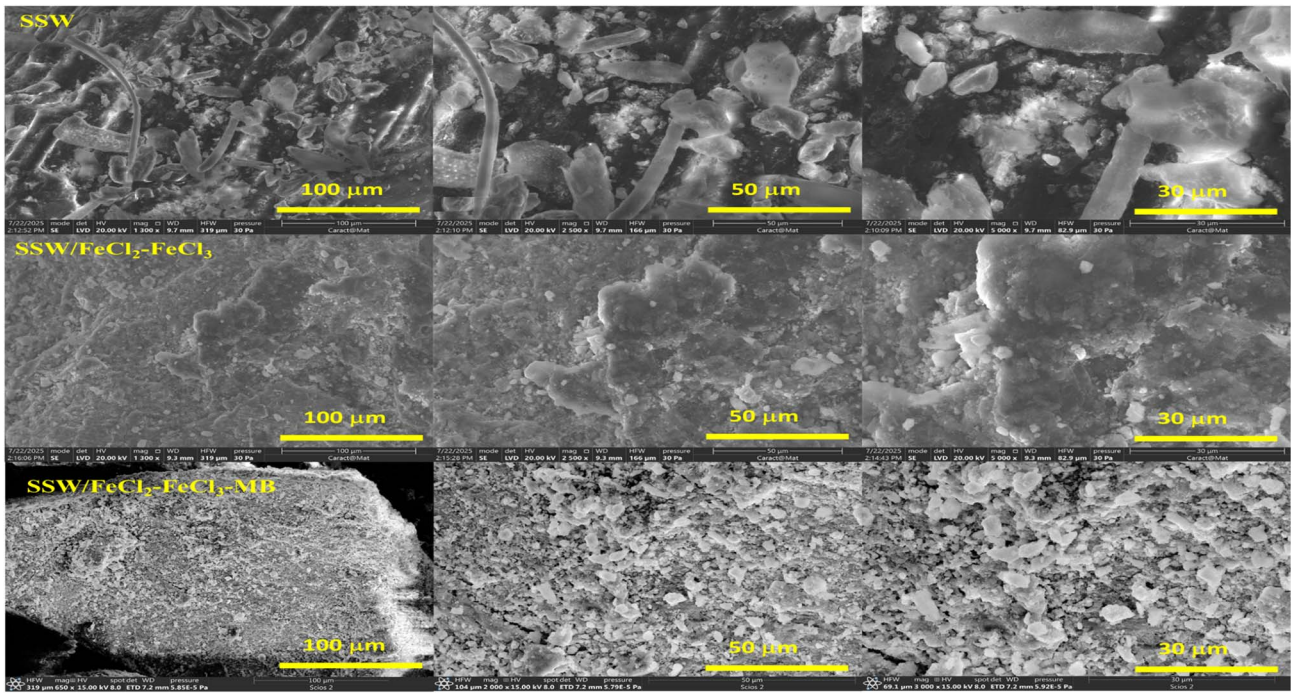

Fig. 3 SEM of SSW, SSW/$FeCl_2$-$FeCl_3$, and SSW/$FeCl_2$-$FeCl_3$-MB at different magnifications.

in untreated biomass.[68,69] After modification with $FeCl_2$–$FeCl_3$, the morphology of SSW/$FeCl_2$-$FeCl_3$ becomes rougher, granular, and amorphous, with the disappearance of the fibrils visible in the raw material, indicating a profound disruption of the matrix and the formation of microporous aggregates associated with the carbonaceous phases and deposited ferric species.[68] The existence of pores on the surface of the biosorbent was confirmed by BET analysis. This transformation is consistent with observations reported in recent work, where chemical activation of shrimp shell waste leads to more developed, rougher surfaces that are conducive to adsorption.[70] Thus, the observed evolution confirms that $FeCl_2$–$FeCl_3$ treatment significantly improves the material's texture and promotes the formation of active sites that can optimize adsorption performance. The SEM micrographs of SSW/$FeCl_2$-$FeCl_3$ after methylene blue adsorption (see the corresponding figures) show a clear modification of the surface topography. The previously well-defined micropores and sharp granular edges appear attenuated, forming a more continuous and compact layer. This change is attributed to the deposition of MB molecules on the SSW/$FeCl_2$-$FeCl_3$ surface and within its internal pore structure. These observations are consistent with the FTIR analysis and confirm that the improved texture and active sites created by the $FeCl_2$–$FeCl_3$ treatment effectively promote the trapping of organic pollutants such as methylene blue.

EDX analysis of the SSW (Fig. 4) shows a high oxygen (O) and carbon (C) content, characteristic of the organo-mineral matrix of shrimp shells, as well as a significant proportion of calcium (Ca) linked to the presence of calcium carbonate ($CaCO_3$),[60] a major component of these biomaterials. After modification with $FeCl_2$–$FeCl_3$, the elemental composition of the SSW/$FeCl_2$-$FeCl_3$ changes significantly, with a decrease in the proportion of C while the Fe fraction increases sharply (24.89 wt%), confirming the incorporation and efficient fixation of ferric species on the SSW surface. The slight increase in Cl also indicates the persistence of chloride anions from the treatment. These results demonstrate the success of the chemical modification.

After methylene blue adsorption, the elemental profile changes significantly, providing direct evidence of the dye's presence. Specifically, the appearance of nitrogen (N) at 2.08 wt% with traces of sulfur (S) serves as molecular signature of the $C_{16}H_{18}ClN_3S$ molecule. Furthermore, the carbon content rises from 7.79% back up to 22.14%, reflecting the accumulation of organic dye molecules on the SSW/$FeCl_2$-$FeCl_3$ surface, while the iron content remains stable at 29.10%, indicating robust chemical modification with no leaching during treatment. These results collectively demonstrate that the modified material provides active sites that successfully capture the cationic dye through surface interactions.

The textural properties of SSW and SSW/$FeCl_2$-$FeCl_3$ were investigated using nitrogen adsorption–desorption analysis, the resulting BET parameters are shown in Fig. 5. Both samples exhibit type IV adsorption–desorption isotherms according to IUPAC classification, which indicates a predominantly mesoporous structure.[72,73] The BET specific surface area increased from 5.22 $m^2\ g^{-1}$ for the raw material to 24.78 $m^2\ g^{-1}$ after modification, confirming the development of additional surface sites.[71,74] Similarly, the total pore volume, calculated from the amount of nitrogen adsorbed at $P/P_0 = 0.99$, increases from 0.019 to 0.097 $cm^3\ g^{-1}$. This reflects the opening of new pores induced by the chemical treatment.[75] The average pore diameter (D_p), determined *via* the BJH method from the desorption branch, decreased slightly from 20.35 to 15.36 nm while remaining well within the mesoporous range (2–50 nm).[76] These

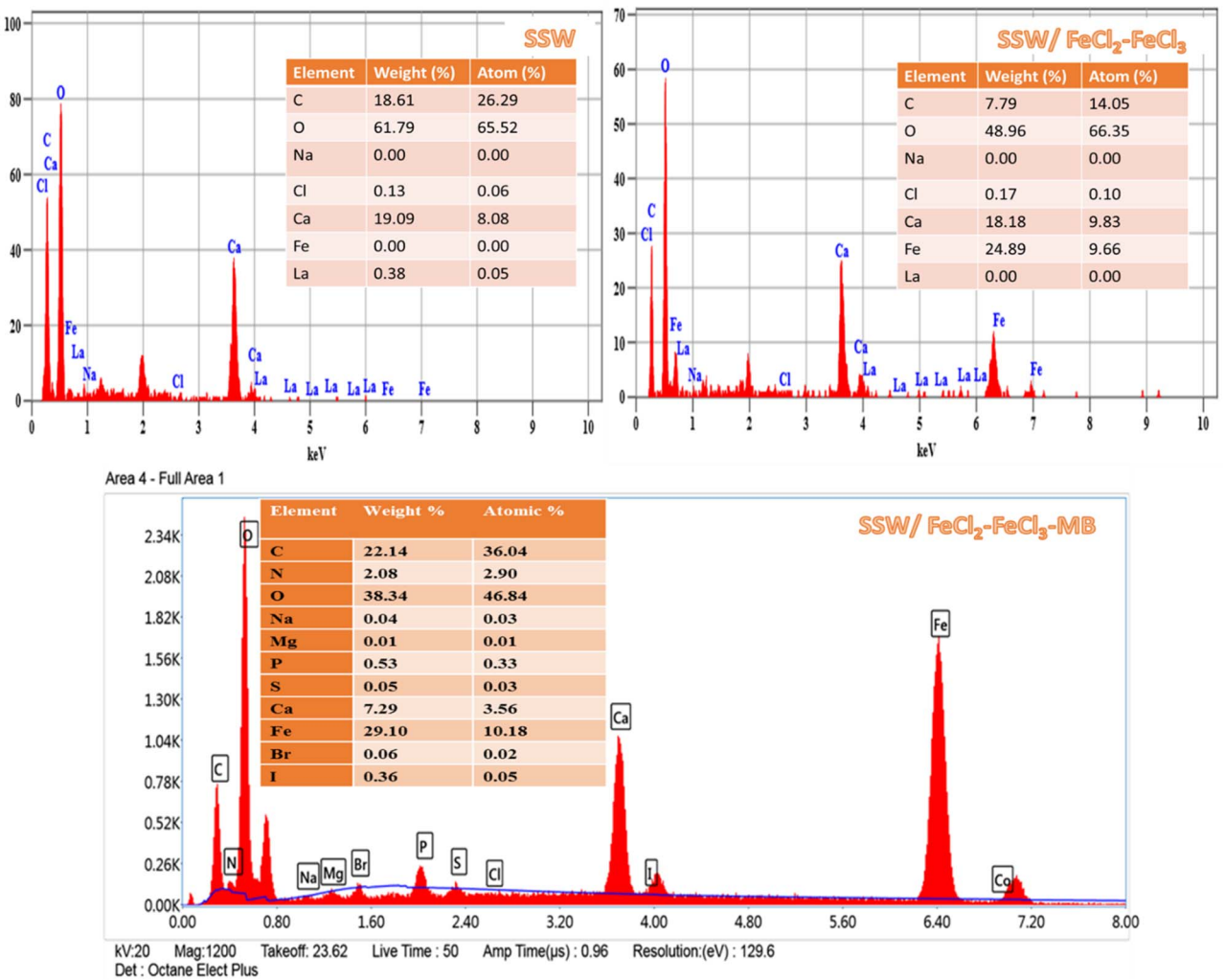

Fig. 4 EDX of SSW, SSW/$FeCl_2$-$FeCl_3$, and SSW/$FeCl_2$-$FeCl_3$-MB samples.

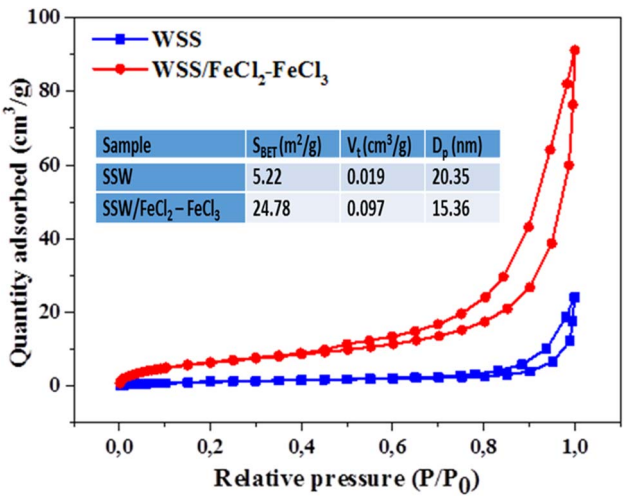

Fig. 5 N_2 adsorption–desorption isotherm of SSW/$FeCl_2$-$FeCl_3$ sample.

enhanced textural properties are expected to improve methylene blue (MB) adsorption by facilitating dye diffusion and increasing the number of accessible active sites. Particle size distribution analysis revealed significant variations depending on chemical modification.

The granulometric parameters obtained by laser diffraction analysis for raw and modified shrimp shell, and shrimp shell after adsorption are summarized in Table 2. This analysis revealed marked variation in size distribution depending on the chemical modification applied. Raw SSW exhibits a coarse distribution with a broad dispersion (SPAN = 2.14), indicating

Table 2 Granulometric parameters of SSW, SSW/$FeCl_2$-$FeCl_3$, and SSW/$FeCl_2$-$FeCl_3$-MB determined by laser diffraction analysis

Samples	D_{10} (µm)	Median (D_{50}) (µm)	D_{90} (µm)	SPAN
SSW	66.2	318	746.3	2.14
SSW/$FeCl_2$-$FeCl_3$	186.5	451	907.5	1.6
SSW/$FeCl_2$-$FeCl_3$-MB	92.24	347.3	810.8	2.07

significant heterogeneity and particle agglomeration. Following chemical modification, the SPAN decreased significantly to 1.60, resulting in a more homogeneous distribution attributed to particle restructuring and the removal of fine fragments during treatment. However, after adsorption of MB, the SPAN increased to 2.07. This suggests particle aggregation and a broader size distribution, likely due to the bridging effects of dye molecules interacting with the functional groups present on the modified SSW surface.[77,78] This increase in SPAN confirms that the adsorption process significantly alters the physical arrangement of the biosorbent particles.

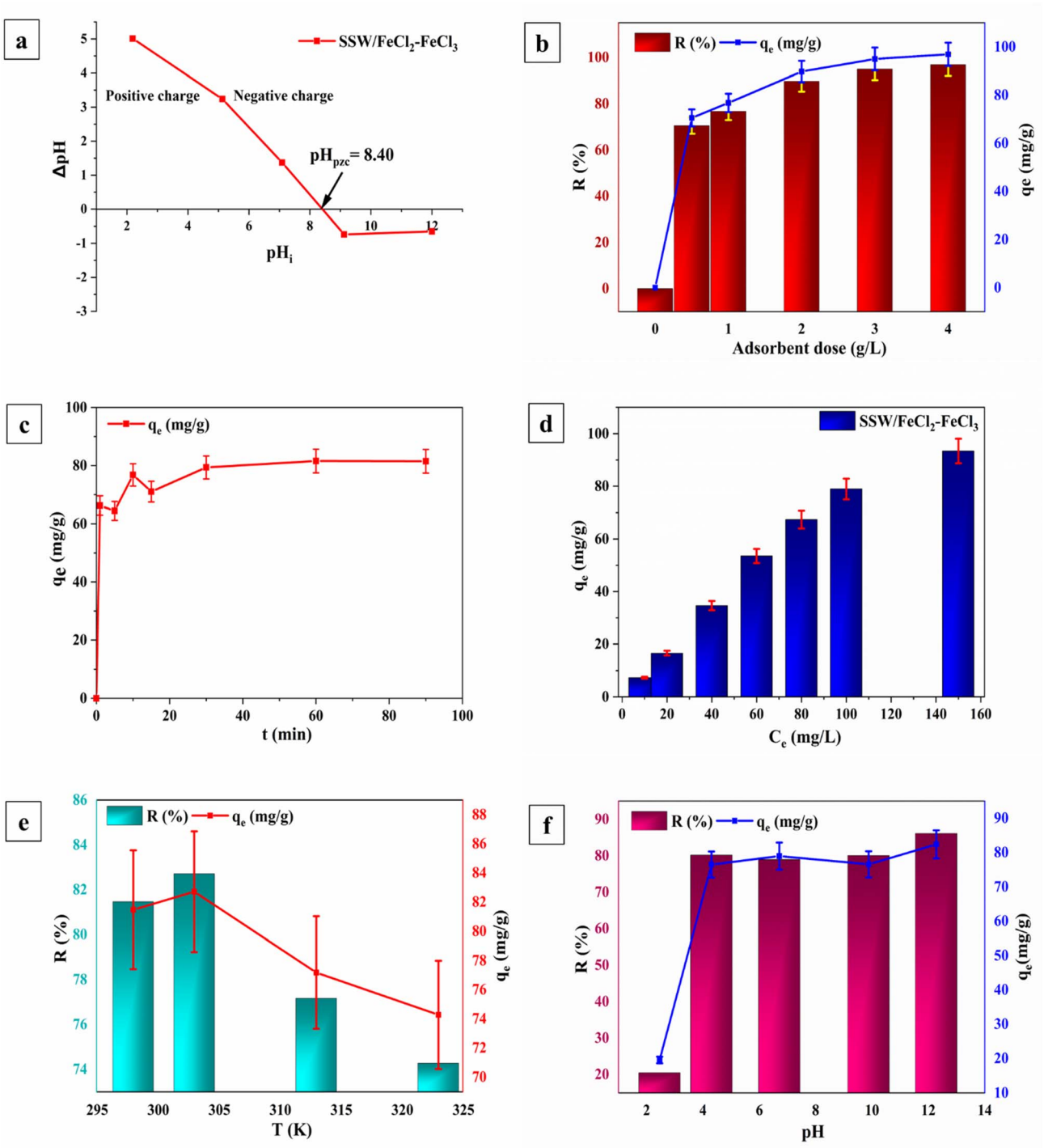

Fig. 6 Adsorption study of MB onto SSW/$FeCl_2$-$FeCl_3$: (a) point of zero charge (pH_{pzc}), (b) effect of adsorbent dose (T = 25 °C, pH solution, C_0 = 100 mg L^{-1}, and t = 90 min), (c) effect of contact time (T = 25 °C, pH solution, C_0 = 100 mg L^{-1}, and m = 0.050 g), (d) effect of initial dye concentration (T = °C, pH solution, m = 0.050 g, and t = 90 min), (e) effect of temperature (m = 0.050 g, pH solution, C_0 = 100 mg L^{-1}, and t = 90 min), and (f) effect of initial pH (T = 25 °C, m = 0.050 g, C_0 = 100 mg L^{-1}, and t = 90 min) on MB removal by efficiency.

The surface charge of an adsorbent material, which results from acid-base equilibria, is fundamentally dependent on the pH and ionic strength of the aqueous solution. This charge can be positive, negative, or neutral depending on the environmental conditions. Experimental results indicate that the point of zero charge (pH_{pzc}) for the SSW/$FeCl_2$-$FeCl_3$ is 8.40 (Fig. 6a); at this specific value, the SSW/$FeCl_2$-$FeCl_3$ surface remains electrically neutral. When the solution pH is below this value (pH < 8.40), particularly in a strongly acidic environment, the oxygenated surface sites of the SSW/$FeCl_2$-$FeCl_3$ become resulting in a net positive surface charge. Conversely, at pH levels above the pH_{pzc} (pH > 8.40) in basic media, the dissociation of hydroxylated functional groups occurs. This deprotonation leads to the appearance of negatively charged sites, causing the overall surface to become negatively charged. Therefore, the pH_{pzc} serves as critical threshold for understanding the electrostatic interactions between the adsorbent and the target dye molecules.

The modification of shrimp shell waste (SSW) with $FeCl_2$/$FeCl_3$ leads to the development of a multifunctional composite with enhanced active sites for methylene blue (MB) adsorption. The BET analysis confirms a significant structural improvement, with the specific surface area increasing from 5.22 to 24.78 $m^2\ g^{-1}$ and the total pore volume rising from 0.019 to 0.097 $cm^3\ g^{-1}$, thereby creating new physical active sites through mesopore formation. Furthermore, FTIR spectra reveal that the iron-based modification introduces Lewis acid sites (iron oxyhydroxides) and shifts oxygen-containing functional groups (–OH, C=O, and CO_3^{2-}). These groups act as chemical active sites that facilitate MB removal through a combination of electrostatic attraction (between the cationic dye and negatively charged surface), complexation/coordination with iron centers, and hydrogen bonding with the chitinous matrix.

3.2. Effects of experimental conditions on adsorption of MB

The adsorption study of methylene blue onto the SSW/$FeCl_2$-$FeCl_3$ was carried out under various operating conditions: optimal mass, contact time, initial concentration, temperature, and pH.

3.2.1. Effect of adsorbent mass. Based on the information provided in Fig. 6b, there is a clear relationship between the adsorbent mass and the dye removal rate. The results indicate that the percentage of dye removal increases with an increasing adsorbent mass. This suggests that a greater adsorbent mass provides a larger number of available adsorption sites, consequently increasing the removal efficiency.[79] However, it is important to note that this relationship reaches a saturation plateau. At this stage, the active sites on the adsorbent surface become fully utilized; therefore, adding more adsorbent does not yield further improvements in dye removal. To optimize the process, it is crucial to balance the amount of adsorbent used and the against the desired removal efficiency. Based on the experiments, a quantity of 0.05 g was selected as the optimal adsorbent mass, providing a satisfactory yield while minimizing the amount of SSW/$FeCl_2$-$FeCl_3$ used.

3.2.2. Effect of contact time. The effect of contact time on the adsorption of BM onto SSW/$FeCl_2$-$FeCl_3$ is illustrated in Fig. 6c. The adsorption capacity (q_e) increased rapidly, reaching a maximum during the first few minutes. The rate then slowed over time until reaching 81.56 mg g^{-1} at 60 min, beyond which no significant change was observed. This adsorption kinetics behavior is attributed to the initial adsorption of methylene blue dye onto the external surface of the SSW/$FeCl_2$-$FeCl_3$. Once the external surface reaches the saturation, the dye molecules diffuse into the pores of the adsorbent and are subsequently adsorbed by the internal surface. Although equilibrium was reached after approximately 60 min, a contact time of 90 min was selected for subsequent experiments (pH, initial concentration, adsorbent dose, *etc.*). This extended contact time ensures that complete equilibrium is attained under all experimental conditions, minimizing kinetic limitations and allowing for an accurate evaluation of other parameters.

3.2.3. Effect of initial dye concentration. The influence of initial methylene blue (MB) concentration on the adsorption capacity of SSW/$FeCl_2$-$FeCl_3$ was investigated within the range of 10–150 mg L^{-1} (Fig. 6d).

As shown, the adsorption capacity increased significantly from 7.31 mg g^{-1} at 10 mg L^{-1} to 93.36 mg g^{-1} at 150 mg L^{-1}. This enhancement in adsorption capacity with increasing dye concentration can be attributed to the higher driving force of mass transfer, which facilitates the diffusion of MB molecules onto the active sites of the adsorbent surface.

At lower initial concentrations (10–20 mg L^{-1}), numerous active sites are available on the adsorbent surface; however, the adsorption capacity remains relatively low due to limited dye–adsorbent interactions. As the concentration increases (40–100 mg L^{-1}), more MB molecules compete for the available sites, leading to a sharp rise in q_e. Beyond 100 mg L^{-1}, the increase becomes less pronounced, indicating that the surface active sites are progressively saturated and that equilibrium between adsorption and desorption is being reached. These results demonstrate that the adsorption process is highly dependent on the initial dye concentration, as it determines the driving for mass transfer between the aqueous phase and the adsorbent surface.

3.2.4. Effect of temperature. Based on the results shown in Fig. 6e, was observed that the adsorption capacity of the SSW/$FeCl_2$-$FeCl_3$ decreased as the temperature increased from 25 °C to 50 °C. This indicates that higher temperatures do not favor the adsorption of methylene blue (MB) onto the surface. The inverse relationship between temperature and adsorption capacity suggests that the process is exothermic. Consequently, the optimal temperature for this study was determined to be room temperature (25 °C).

3.2.5. Effect of pH. The pH of the solution significantly influences both the surface charge of the absorbent and the degree of dissociation of the solute. As illustrated in Fig. 6f, the adsorption capacity increases with increasing pH. This improvement can be explained by the point of zero charge ($pH_{pzc} = 8.4$) of the SSW/$FeCl_2$-$FeCl_3$ composite and the surface charge of the adsorbent. At very acidic pH, the adsorbent

surface is strongly protonated, which limits electrostatic attraction and results in low adsorption capacity due to repulsion with the cationic MB.[80] At pH values between ~4 and 8.4, although the surface remains largely positively charged, adsorption remains high because of non-electrostatic interactions such as hydrogen bonding and π–π interactions between the dyes aromatic rings and functional groups on the SSW/$FeCl_2$-$FeCl_3$ surface that facilitate MB uptake. At pH > 8.4, the surface of the SSW/$FeCl_2$-$FeCl_3$ becomes negatively charged, which promotes the adsorption of the cationic dye, methylene blue, through electrostatic attraction.[27,80] However, a slight decrease in adsorption capacity observed around pH_{10} may be attributed to competition between MB^+ and OH^- ions for adsorption sites.[81]

At pH_{12}, the adsorption capacity (82.36 mg g^{-1}) increases again. This behavior may be explained by extensive deprotonation of surface functional groups, including iron hydroxide groups introduced during the modification process, which increases the negative surface charge and strengthens electrostatic attraction toward MB^+.[82]

Therefore, the neutral pH was selected for the subsequent adsorption experiments because it provides high adsorption efficiency while representing environmentally relevant conditions for wastewater treatment.

3.3. Kinetics modeling

The parameters for the PFO, PSO, Elovich and IPD models are summarized in Table S3 and shown in Fig. 7a and b. For the PFO model, the calculated adsorption capacity ($q_{e,calc}$ = 75.78 mg g^{-1}) was slightly lower than the experimental value ($q_{e,exp}$ = 81.47 mg g^{-1}), with a determination coefficient (R^2) of 0.9478, indicating a moderate fit. In contrast, the PSO model

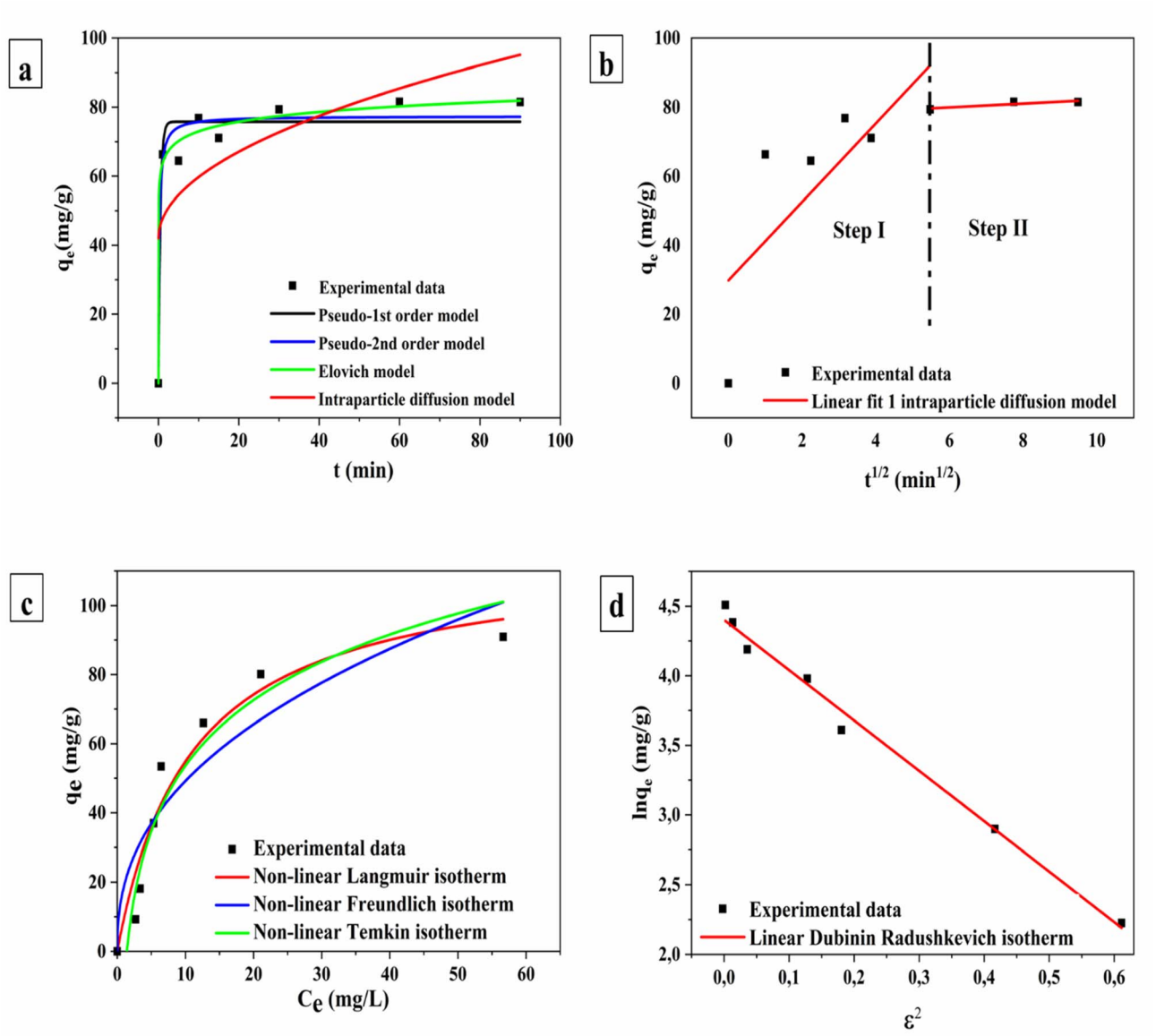

Fig. 7 Non-linear (a) adsorption kinetics of PFO, PSO and IPD models; (b) linear IPD kinetic plot; (c) adsorption isotherms of Langmuir, Freundlich, and Temkin models; (d) linear of D–R isotherm for MB removal onto SSW/$FeCl_2$-$FeCl_3$.

provided better agreement between experimental and calculated values ($q_{e,calc}$ = 77.38 mg g^{-1}), achieving a higher correlation coefficient of R^2 = 0.9604. This suggests that the adsorption process follows pseudo-second-order kinetics, implying that the rate-limiting step involve chemisorption through valence forces or electron exchange between the adsorbate and the adsorbent surface. The Elovich model showed an excellent correlation (R^2 = 0.9835), suggesting that the adsorption surface is highly heterogeneous and involves multiple types of active sites. The high initial adsorption rate ($\alpha = 2.65 \times 10^7$) confirms a rapid fixation of dye molecules at the beginning of the process, followed by a progressive slowdown as the active sites become saturated. The kinetic mechanisms were further investigated using the Weber–Morris intraparticle diffusion (IPD) model. Initially, the non-linear global fit of the IPD model exhibited a low correlation coefficient (R^2 = 0.3655), demonstrating that a single-stage diffusion mechanism cannot fully describe the adsorption process. To provide a more accurate interpretation, a multi-linear analysis was performed by plotting q_t *versus* $t^{1/2}$ (Fig. 7b). As shown in the multi-linear plot, the adsorption process proceeds through two distinct stages. The first stage corresponds to the external surface adsorption (film diffusion), where the dye molecules move from the solution to the adsorbent surface. The significant positive intercept (C = 29.81 mg g^{-1}) indicates that the regression line does not pass through the origin, confirming that intraparticle diffusion is not the sole rate-limiting step; boundary layer resistance also plays a critical role. The second stage represents progressive intraparticle diffusion into the internal macro- and micropores of the SSW/$FeCl_2$-$FeCl_3$. Finally, the gradual decrease in the slope (from 11.37 to 0.548) as the system approaches equilibrium indicates the saturation of available active sites. Overall, these kinetic results confirm that MB adsorption onto SSW/$FeCl_2$-$FeCl_3$ is best described by the pseudo-second-order (PSO) and Elovich models, which highlight the dominant roles of chemisorption and surface heterogeneity alongside internal diffusion.

3.4. Isotherms of MB adsorption

The equilibrium data for methylene blue (MB) adsorption onto SSW/$FeCl_2$-$FeCl_3$ were analyzed using the nonlinear forms of the Langmuir, Freundlich, Temkin models, and the linear from of the Dubinin–Radushkevich (D–R) model. The corresponding parameters are summarized in Table S4 and shown in Fig. 7c and d.

The Langmuir model showed good agreement with the experimental data (R^2 = 0.9344), indicating monolayer adsorption on a homogeneous surface with identical, energetically equivalent active sites. The maximum adsorption capacity (q_m) was 114.47 mg g^{-1}, reflecting strong affinity of SSW/$FeCl_2$-$FeCl_3$ for MB molecules. Furthermore, the calculated R_L values ranged from 0.098 to 0.521, confirming favorable adsorption.

The Freundlich isotherm parameter $1/n = 0.415$ ($1/n < 1$) also indicates favorable adsorption of MB onto the modified SSW, with good affinity of the dye molecules for the adsorbent surface.[81] However, the lower correlation coefficient (R^2 = 0.8362) suggests that the Freundlich model provides a less accurate description of the adsorption equilibrium.

The Temkin model also provided a good fit ($R^2 \simeq 0.94$), reflecting significant adsorbate–adsorbent interactions. The Temkin constants (B_T = 27.37 J mol^{-1} and K_T = 0.709 L g^{-1}) suggest that the heat of adsorption decreases linearly with increasing coverage, indicating chemisorption tendencies due to adsorbate–adsorbent bonding effects.

The parameters of the D–R model were determined using its linear form, by plotting $\ln(q_e)$ as a function of the Polanyi potential (ε^2). The D–R isotherm yielded the highest correlation coefficient (R^2 = 0.9879), implying that it best describes the equilibrium adsorption process. The calculated mean free energy (E) value was 0.372 kJ mol^{-1}, well below the 8 kJ mol^{-1} threshold, indicating that MB adsorption onto SSW/$FeCl_2$-$FeCl_3$ is mainly governed by physisorption through weak electrostatic forces and van der Waals interactions. The theoretical monolayer capacity (q_{mDR} = 81.45 mg g^{-1}) is consistent with the Langmuir value, confirming the reliability of the results. The strong fit of the Temkin and D–R models suggests that while physical adsorption is the dominant mechanism, minor chemisorptive contributions may also be present.

3.5. Adsorption thermodynamic

The thermodynamic parameters namely Gibbs free energy (ΔG°), standard enthalpy (ΔH°) and standard entropy (ΔS°), were evaluated to determine the spontaneity and thermal nature of the adsorption process. Regarding the calculation of thermodynamic parameters, we carefully considered the methodology suggested by Saad *et al.* (2025).[83] However, we opted to utilize the distribution coefficient ($K_D = q_e/C_e$) as the basis for our thermodynamic study rather than the Langmuir constant (K_L). While the Langmuir model is widely used, it proved less suitable for our specific system across the investigated temperature range. It is important to note that for many adsorption systems, particularly those involving complex interactions or non-ideal behavior, the K_D approach remains a robust and standard convention. This choice is supported by a significant body of recent literature in the field of environmental chemistry, which advocates for the use of K_D to ensure that the resulting thermodynamic constants accurately reflect the experimental distribution of the solute at equilibrium.[84–88]

ΔG° was calculated using eqn (16) and cross-checked *via* the relation (17):[89–92]

$$\Delta G^\circ = \Delta H^\circ - T\Delta S^\circ \quad (16)$$

$$\Delta G^\circ = -RT \ln K_D \quad (17)$$

By combining these, the van't Hoff equation ($\ln K_D$) is expressed as:

$$\ln K_D = \frac{\Delta S^\circ}{R} - \frac{\Delta H^\circ}{RT} \quad (18)$$

Table 3 Thermodynamic parameters for the adsorption of MB onto SSW/$FeCl_2$-$FeCl_3$ at different temperatures

T (°K)	$\Delta H°$ (kJ mol^{-1})	$\Delta S°$ (J mol^{-1} K^{-1})	$\Delta G°$ (kJ mol^{-1})
298	−16.54	−44.33	−3.33
303			−3.11
313			−2.67
323			−2.22

where: R is the universal gas constant (8.314 J mol^{-1} K^{-1}), T (K) is the absolute temperature, and K_D (L g^{-1}) represents the distribution coefficient, which is calculated by eqn (19):[87,88]

$$K_D = \frac{q_e}{C_e} \quad (19)$$

$\Delta H°$ and $\Delta S°$ were determined from the van't Hoff plot ($\ln K_D$ *versus* $1/T$), where the slope and intercept correspond to $-\Delta H°/R$ and $\Delta S°/R$, respectively. The calculated thermodynamic parameters are summarized in Table 3 and shown in Fig. 8. The negative values of $\Delta G°$ confirm that the adsorption process is thermodynamically spontaneous. Furthermore, the decrease in the magnitude of $\Delta G°$ with increasing temperature indicates that the adsorption of methylene blue (MB) onto SSW/$FeCl_2$-$FeCl_3$ becomes less favorable at higher temperatures. The negative enthalpy value ($\Delta H° = -16.54$ kJ mol^{-1}) demonstrates that the process is exothermic. Its relatively low magnitude ($\Delta H°$ < 40 kJ mol^{-1}) suggests that the adsorption is primarily governed by physical interactions, such as van der Waals forces and electrostatic attractions, rather than chemical bonding,[93,94] which is consistent with the D–R isotherm model. Additionally, the negative entropy change ($\Delta S° = -44.33$ J mol^{-1} K^{-1}) indicates a decrease in randomness at the solid–liquid interface during adsorption. This reduction in entropy can be attributed to the arrangement of MB molecules on the adsorbent surface, which become more ordered and less mobile upon adsorption. Overall, the adsorption of methylene blue onto SSW/$FeCl_2$-$FeCl_3$ is a spontaneous, exothermic process accompanied by decreased system entropy, reflecting enhanced molecular organization at the adsorbent interface.

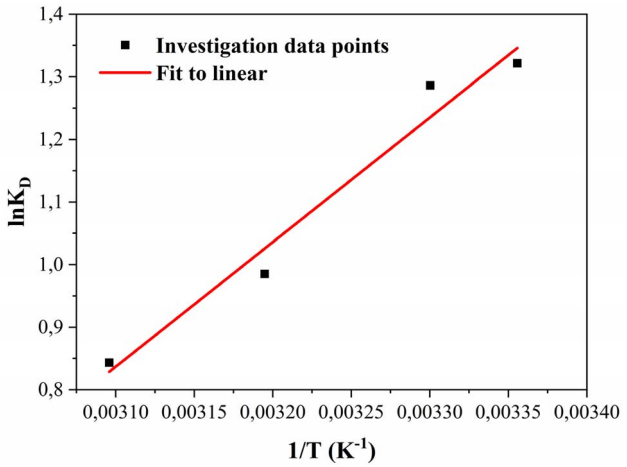

Fig. 8 Plot of the van't Hoff equation.

The interpretation of the adsorption mechanism of MB onto the SSW/$FeCl_2$-$FeCl_3$ composite reveals a complex, dual process. On one hand, the low mean free energy ($E = 0.372$ kJ mol^{-1}) from the Dubinin–Radushkevich model, combined with the negative enthalpy change ($\Delta H° = -16.54$ kJ mol^{-1}), confirms the dominance of physisorption governed by electrostatic interactions and van der Waals forces. On the other hand, the strong fit to the pseudo-second-order kinetic model ($R^2 = 0.9604$) and, especially, the excellent correlation with the Elovich model ($R^2 = 0.9835$), which is tailored for chemisorption on heterogeneous surfaces, indicate a concurrent chemical contribution. Overall, these findings suggest a physically dominant mechanism augmented by specific interactions between the modified biosorbent's active sites and dye molecules.[95]

3.6. Design of experiments by BBD

The ANOVA results presented in Table 4 demonstrate that the main effects of all variables (A, B, and C), as well as the two-factor interaction between pH and initial MB dye concentration (AB), are statistically significant model terms influencing the BBD response for MB adsorption using SSW/$FeCl_2$-$FeCl_3$. Additionally, the analysis indicates that the effects of variables A

Table 4 ANOVA results for the adsorption capacity of MB dye onto SSW/$FeCl_2$-$FeCl_3$ using a Box–Behnken design[a]

Source	Sum of squares	df	Mean square	F-Value	p-Value	
Model	21 101.34	5	4220.27	134.82	< 0.0001	Significant
A-Concentration	17 281.08	1	17 281.08	552.07	< 0.0001	
B-pH	2550.73	1	2550.73	81.49	< 0.0001	
C-Temperature	305.70	1	305.70	9.77	0.0097	
AB	666.31	1	666.31	21.29	0.0007	
A^2	297.52	1	297.52	9.50	0.0104	
Residual	344.33	11	31.30			
Lack of fit	344.33	7	49.19			
Pure error	0.0000	4	0.0000			
Cor total	21 445.67	16				

[a] df = degree of freedom.

Table 5 Regression coefficients and statistical validation of the BBD model[a]

Std dev.	Mean	C.V. %	R^2	Adjusted R^2	Predicted R^2	Adeq. precision
5.59	56.92	9.83	0.9839	0.9839	0.9462	39.08

[a] R^2: determination coefficient, Adeq. precision: adequate precision, Std dev.: standard deviation.

and B are independent of factor C, while A and B exhibit a significant interactive effect, confirming their mutual dependence. The BBD model developed for predicting the equilibrium adsorption capacity of MB was deemed statistically valid. The final regression model, expressed in terms of coded variables, is given by the following equation:

$$\text{MB adsorption} = +60.89 + 46.48A + 17.86B - 6.18C + 12.91AB - 8.38A^2 \quad (20)$$

The correlation coefficients (R^2 and adjusted R^2) of the BBD model, presented in Table 5, are both close to unity, indicating strong agreement between the predicted and experimental data. Specifically, the R^2 value of 0.9839 for the SSW/$FeCl_2$-$FeCl_3$ adsorbent confirms the robustness and reliability of the developed statistical model. The proximity of the adjusted R^2 to the R^2 further supports the model's suitability and predictive accuracy. Model significance was also confirmed by the high F-value (134.82) associated with the equilibrium adsorption capacity of MB onto SSW/$FeCl_2$-$FeCl_3$. Furthermore, the low p-value ($p < 0.05$) reinforces the statistical significance of the model and its terms. The response surface methodology employs three-dimensional plots to illustrate the interaction effects among independent variables, allowing for a clearer understanding of their combined influence on the response. Complementarily, two-dimensional contour plots provide a visual map of the predicted response values, aiding in the identification of optimal conditions within the experimental design space.[96] According to the quadratic model described in eqn (19), both three-dimensional and contour plots (Fig. 9) were generated to visualize the effects of the process variables. As illustrated in Fig. 9, initial dye concentration and pH emerge as the most influential factors affecting the response. Specifically, MB adsorption increases as the pH increases, as evidenced by the color shift from blue to red, which indicates a transition from lower (~20 mg g^{-1} at pH_4) to higher adsorption levels (114 mg g^{-1} at pH_{10-12}). Additionally, increasing the initial MB dye concentration from 10 to 150 mg L^{-1} led to a corresponding rise in the adsorption capacity (q_e from ~20 to 114.47 mg g^{-1}, 0.050 g adsorbent, 25 °C). The significant interaction between pH and initial concentration (3D surface plot, Fig. 9) can be explained as follows: as the initial concentration increases from 10 to 150 mg L^{-1}, the adsorption capacity increases significantly. However, this positive effect is intensified at basic pH (pH_{10}), due to deprotonation of functional groups enhancing electrostatic attraction towards cationic MB molecules. When combined with high initial concentration (providing a strong

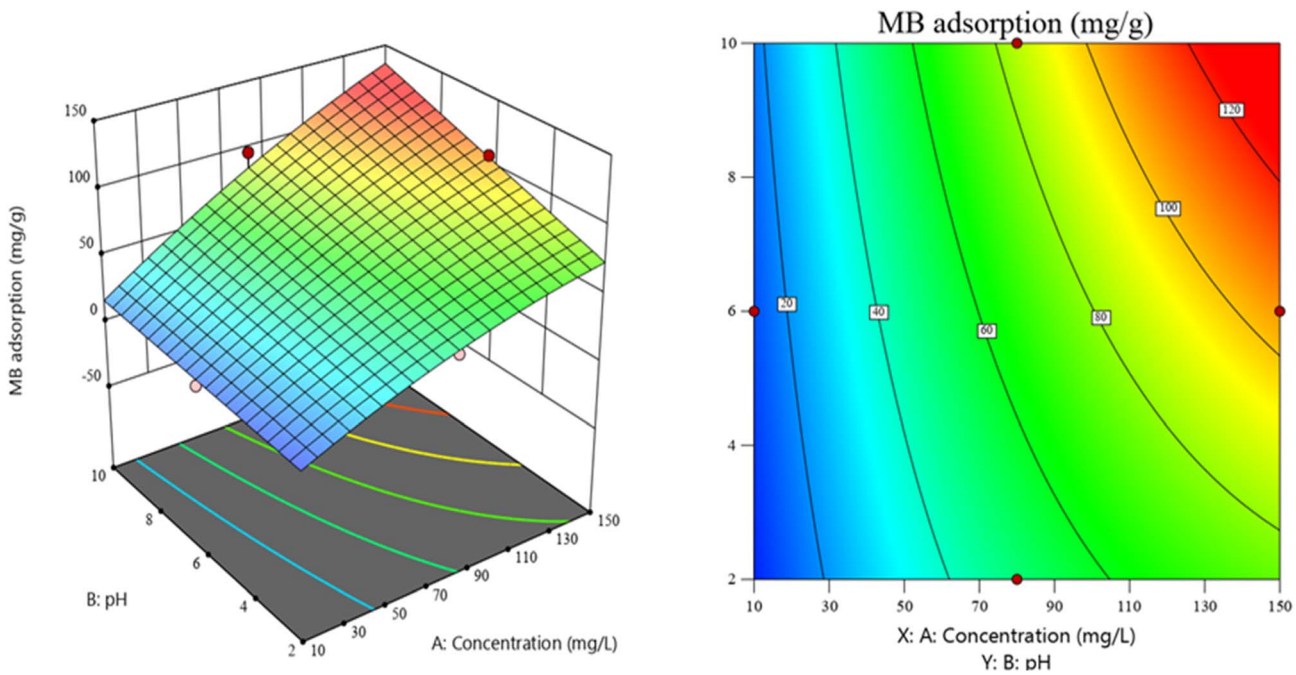

Fig. 9 Contour and response surface plots for MB adsorption onto SSW/$FeCl_2$-$FeCl_3$: influence of pH and initial dye concentration.

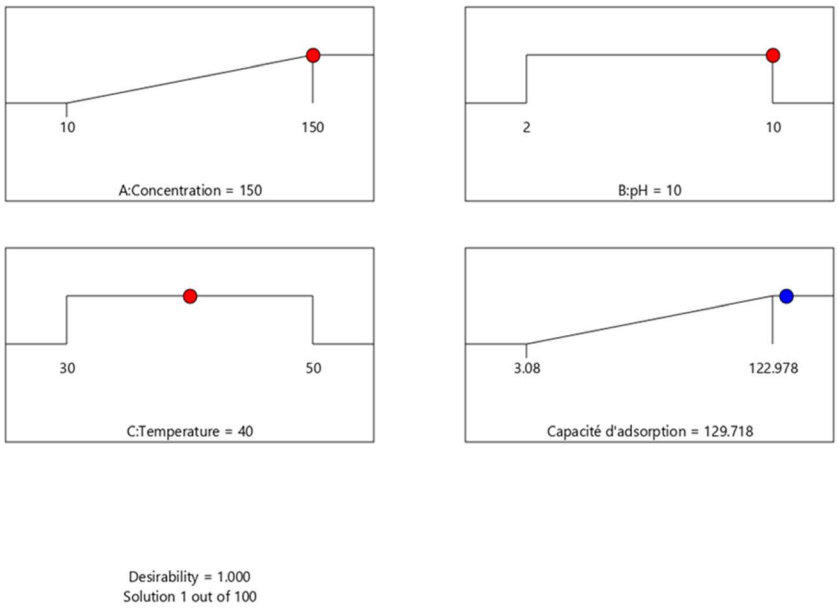

Fig. 10 Optimization of MB adsorption capacity on SSW/$FeCl_2$-$FeCl_3$ using the desirability function approach.

driving force), the synergistic effect leads to maximum adsorption capacity.

The optimization diagram based on the BBD design is presented in Fig. 10. These diagrams illustrate the optimal conditions required to maximize the adsorption capacity of MB dye onto SSW/$FeCl_2$-$FeCl_3$. According to the model, the optimal parameters for achieving maximum adsorption are an initial dye concentration of 150 mg L^{-1}, a pH of 10, and a temperature of 40 °C. Under these conditions, the predicted maximum adsorption capacity is 129.72 mg g^{-1}. The associated desirability value of 1.000 confirms that the optimal experimental conditions closely match the model predictions, thereby validating the effectiveness of the RSM approach in optimizing the adsorption process using SSW/$FeCl_2$-$FeCl_3$.

3.7. Comparison of adsorption conditions and performance

The adsorption performance for methylene blue (MB) was evaluated by comparing key operating parameters and

Table 6 Comparison of adsorption conditions and maximum adsorption capacities of various adsorbents for MB

Adsorbent	S_{BET} (m^2 g^{-1})	t (min)	T (°C)	pH	Adsorbent dosage	Isotherm	q_{max} (mg g^{-1})	Ref.
Chi-AA	—	30	—	12	0.1 g	Freundlich	1.756	97
Chi-AA-IS	—	5	—	10	0.1 g	Langmuir	4.69	
AC	—	120	60	5	10 g L^{-1}	Langmuir	5.03	98
Chitosan	4.076	30	RT	9	1 g	Langmuir	7.605	84
Chitosan hydrogels/sunflower husks	17.533	120	—	8	4 g L^{-1}	Freundlich	11.32	99
CS/SiO_2	640.37	40	35	7	6 g L^{-1}	Langmuir	13.97	100
AC/CH composite	610.31	60	25	6.5	0.1 g	Langmuir	22.52	28
CS/Mt-OREC	—	—	—	6	6 g L^{-1}	Langmuir	24.69	101
ZnO-g-C_3N_4@(CMCH/ALG-g-PAA)	—	145	—	8	1 g L^{-1}	Langmuir, Temkin, sips, and Redlich–Peterson	34.59	102
Shrimp shells/NO_3	—	105	120	10	10 g L^{-1}	—	48.83	103
CCH	254.17	55	RT	7	120 g L^{-1}	Langmuir	72.19	104
Algae biomass/silica-magnetite	—	60	—	6	2.50 g L^{-1}	Freundlich	90.90	105
CH	273.56	55	RT	7	120	Langmuir	92.45	104
MCM-48-Cu (BDC-NH_2)/CS hydrogel@Fe_3O_4	137.217	55.51	—	8.49	0.95 g L^{-1}	Freundlich	99.1	106
Poly(HEMA-*co*-IA) magnetic hydrogel (MHG-10)	0.4240	10	RT	6.8	1 g L^{-1}	Langmuir	174.99	82
SpCB	—	1200	20	11.6	2.4 g L^{-1}	Langmuir (physical)	212.77	107
The grafted cross-linked chitosan bead (GCCH)	380.22	55	RT	7	120	Langmuir	128.67	104
SSW/$FeCl_2$-$FeCl_3$	24.78	90	25	7	1 g L^{-1}	D–R	114.47	This study

maximum adsorption capacity (q_{max}) of the SSW/$FeCl_2$-$FeCl_3$ adsorbent with various literature-reported materials, as summarized in Table 6. The most striking finding is the q_{max} of 114.47 mg g^{-1} achieved by the synthesized SSW/$FeCl_2$-$FeCl_3$ modified adsorbent. This substantially surpasses conventional and modified adsorbents, being nearly 22 times higher than standard activated carbon (5.03 mg g^{-1}) and outperforming complex composites such as ZnO-g-C_3N_4 (34.59 mg g^{-1}) and AC/CH (22.52 mg g^{-1}). These results indicate that the iron-salt modification ($FeCl_2$/$FeCl_3$) generates highly efficient active sites for pollutant uptake, superior to simple carbon or chitosan matrices.

Beyond raw capacity, the adsorbent exhibits exceptional efficiency under ambient conditions. Unlike shrimp shells/NO_2 or certain activated carbons requiring elevated temperatures (60–120 °C), it achieves peak performance at 25 °C. Moreover, its optimal effectiveness at pH 7 provides a key advantage for real-world wastewater treatment, eliminating costly and hazardous pH adjustments and enabling a practical "plug-and-play" solution for neutral effluents. The rapid adsorption kinetics and high efficiency observed in this study suggest that the modified shrimp shell is both a highly effective and sustainable low-cost adsorbent for the removal of methylene blue from aqueous solutions.

This material further embodies waste-to-wealth principles by utilizing shrimp shell waste (SSW) as a low-cost precursor, aligning with circular economy goals and outperforming synthetic polymers economically. The iron-salt modification likely imparts magnetic properties, facilitating rapid separation from treated water using an external magnetic field a major operational upgrade over non-magnetic powders. Overall, the synergy of high capacity, neutral pH operation, low-temperature requirements, cost-effectiveness, and ease of recovery positions SSW/$FeCl_2$-$FeCl_3$ as a sustainable, scalable candidate for large-scale water remediation.

4. Conclusion

In this study, a novel biopolymer based on shrimp shells modified with $FeCl_2$–$FeCl_3$ was successfully synthesized and evaluated as an efficient, sustainable adsorbent for removing methylene blue (MB) from aqueous solutions. Physicochemical characterization confirmed the effective incorporation of iron (24.89 wt%, EDX). BET analysis revealed a mesoporous structure with a specific surface area of 24.78 m^2 g^{-1}, a pore volume of 0.097 cm^3 g^{-1}, and an average pore diameter of 15.36 nm. The adsorbent displayed a point of zero charge (pH_{pzc}) of 8.4, facilitating electrostatic attraction of the cationic dye in alkaline media. Batch adsorption experiments demonstrated that equilibrium was reached within 90 min at 25 °C with a dosage of 1 g L^{-1}, achieving a maximum adsorption capacity of 114.47 mg g^{-1}. Kinetic data were best described by the Elovich model, suggesting adsorption on energetically heterogeneous surfaces. Equilibrium data followed the Dubinin–Radushkevich isotherm, indicating a predominantly physical adsorption. Thermodynamic analysis revealed that the MB adsorption process was spontaneous and exothermic. Process optimization using a Box–Behnken design under response surface methodology showed high model predictability (R^2 = 0.98). Under optimal conditions (initial concentration of 150 mg L^{-1}, pH = 10, and T = 40 °C), the adsorption capacity increased to 129.718 mg g^{-1}. These findings confirm that SSW/$FeCl_2$-$FeCl_3$ serves as a high-performance, low-cost and eco-friendly adsorbent for advanced wastewater treatment applications. These findings confirm that SSW/$FeCl_2$-$FeCl_3$ serves as a high-performance, low-cost, and eco-friendly adsorbent for advanced wastewater treatment applications. While the results obtained for methylene blue in simple aqueous solutions are promising, they remain preliminary for industrial-scale use. Future research will focus on evaluating the adsorbent's potential in remediating real textile wastewater to assess matrix effects from multi-metal ions, chemical additives, and complex effluents on adsorption efficiency. Additional studies on regeneration cycles, long-term stability, column operations, and comparative performance against commercial chitosan-based materials are planned to validate its practical viability for textile industry wastewater treatment.

Conflicts of interest

The authors declare (s) that there is no conflict of interest.

Data availability

All data supporting the findings of this study are included within the article and its supplementary information (SI). Supplementary information: additional experimental details. See DOI: https://doi.org/10.1039/d6ra01393g.

References

1 R. K. Mishra and S. C. Dubey, Fresh water availability and its global challenge, *Int. J. Eng. Sci. Invention Res. Dev.*, 2015, **2**(6), 351–407, DOI: 10.58489/2836-5933/004.
2 A. Tariq and A. Mushtaq, Untreated wastewater reasons and causes: A review of most affected areas and cities, *Int. J. Chem. Biol. Sci.*, 2023, **23**(1), 121–143.
3 Md. G. Uddin, S. Nash and A. I. Olbert, A review of water quality index models and their use for assessing surface water quality, *Ecol. Indic.*, 2021, **122**, 107218, DOI: 10.1016/j.ecolind.2020.107218.
4 H. Ben Slama, A. C. Bouket, Z. Pourhassan, F. N. Alenezi, A. Silini, H. Cherif-Silini, T. Oszako, L. Luptakova, P. Golińska and L. Belbahri, Diversity of synthetic dyes from textile industries, discharge impacts and treatment methods, *Appl. Sci.*, 2021, **11**, 6255, DOI: 10.3390/app11146255.
5 P. O. Oladoye, T. O. Ajiboye, E. O. Omotola and O. J. Oyewola, Methylene blue dye: Toxicity and potential elimination technology from wastewater, *Results Eng.*, 2022, **16**, 100678, DOI: 10.1016/j.rineng.2022.100678.
6 D. Mikucioniene, D. Mínguez-García, Md. R. Repon, R. Milašius, G. Priniotakis, I. Chronis, K. Kiskira, R. Hogeboom, R. Belda-Anaya and P. Díaz-García,

Understanding and addressing the water footprint in the textile sector: A review, *Autex Res. J.*, 2024, **24**(1), 1–27, DOI: 10.1515/aut-2024-0004.

7 G. L. Rorissa, E. A. Tesema, R. P. D. M. Reddy, A. R. Hunde, S. Y. Beyena, M. A. Biru, D. T. Mekonnen and T. L. Adnualem, Removal of methylene blue dye from textile industry wastewater using green synthesized teff straw assisted ZnO nanoparticle, *Sci. Rep.*, 2025, **15**, 26230, DOI: 10.1038/s41598-025-11746-9.

8 M. A. Talha, H. E. Agwa, A. M. Beltagi, E. El-Mohsnawy and A. S. Ali, Mechanistic insights into methylene blue biodegradation by Tetradesmus obliquus: A multimodal approach using absorption, fluorescence, and square wave voltammetry, *Sci. Rep.*, 2025, **15**(1), 32663, DOI: 10.1038/s41598-025-19675-3.

9 Y. N. Teixeira, F. J. de Paula Filho, V. P. Bacurau, J. M. C. Menezes, A. Z. Fan and R. P. F. Melo, Removal of methylene blue from a synthetic effluent by ionic flocculation, *Heliyon*, 2022, **8**(10), e10868, DOI: 10.1016/j.heliyon.2022.e10868.

10 S. Ihaddaden, D. Aberkane, A. Boukerroui and D. Robert, Removal of methylene blue (basic dye) by coagulation–flocculation with biomaterials (bentonite and Opuntia ficus indica), *J. Water Process Eng.*, 2022, **49**, 102952, DOI: 10.1016/j.jwpe.2022.102952.

11 A. Nowik-Zajac, I. Zawierucha, J. Łagiewka, K. Jaksender, K. Witt, G. Malina and V. Sabadash, Removal of methylene blue dye from aqueous solutions using polymer inclusion membrane containing calix[4]pyrrole, *Membranes*, 2024, **14**(4), 92, DOI: 10.3390/membranes14040092.

12 M. A. Adelin, G. Gunawan, M. Nur, A. Haris, D. S. Widodo and L. Suyati, Ozonation of methylene blue and its fate study using LC-MS/MS, *J. Phys.: Conf. Ser.*, 2020, **1524**, 012079, DOI: 10.1088/1742-6596/1524/1/012079.

13 M. A. Ali, I. M. Maafa and I. Y. Qudsieh, Photodegradation of methylene blue using a UV/H_2O_2 irradiation system, *Water*, 2024, **16**(3), 453, DOI: 10.3390/w16030453.

14 K. Dob, D. Zouied, M. Khelfaoui, N. Bouzenad, A. Abdennouri and M. Rouainia, Pulicaria odora ethanolic extract as a corrosion inhibitor and its eco-friendly synthesis of CuO nanoparticles for photocatalytic and antimicrobial properties, *Chem. Biochem. Eng. Q.*, 2025, **39**(3), 157–166, DOI: 10.15255/CABEQ.2025.2429.

15 O. Ifguis, Y. Ziat, H. Belkhanchi, F. Ammou, A. Moutcine and C. Laghlimi, Adsorption mechanism of methylene blue from polluted water by *Opuntia ficus indica* of Beni Mellal and Sidi Bou Othmane areas: A comparative study, *Chem. Phys. Impact*, 2023, **6**, 100235, DOI: 10.1016/j.chphi.2023.100235.

16 A. Soltani, M. Faramarzi and S. A. Mousavi Parsa, A review on adsorbent parameters for removal of dye products from industrial wastewater, *Water Qual. Res. J.*, 2021, **56**(4), 181–193, DOI: 10.2166/wqrj.2021.010.

17 Q. Hu and L. Hao, Adsorption technologies in wastewater treatment processes, *Water*, 2025, **17**(15), 2335, DOI: 10.3390/w17152335.

18 X. Wu, Y. Lin, Z. Pi and X. Tan, Dual-functional Fe@ZIF-8 for efficient phosphite removal from wastewater: Synergistic peroxymonosulfate activation and adsorption, *Sep. Purif. Technol.*, 2025, **377**, 134236, DOI: 10.1016/j.seppur.2025.134236.

19 Y. Lin, S. Wu, X. Li, X. Wu, C. Yang, G. Zeng, Y. Peng, Q. Zhou and L. Lu, Microstructure and performance of Z-scheme photocatalyst of silver phosphate modified by MWCNTs and Cr-doped $SrTiO_3$ for malachite green degradation, *Appl. Catal., B*, 2018, **227**, 557–570, DOI: 10.1016/j.apcatb.2018.01.054.

20 D. A. Yaseen and M. Scholz, Textile dye wastewater characteristics and constituents of synthetic effluents: A critical review, *Int. J. Environ. Sci. Technol.*, 2019, **16**(2), 1193–1226, DOI: 10.1007/s13762-018-2130-z.

21 N. Bouzenad, N. Ammouchi, A. Abdennouri, A. Bouzana, H. A. Rudayni, F. Boufahja and H. Bendif, Comprehensive review of alginate: Sources, synthesis, and application in the food packaging sector, *Ital. J. Food Sci.*, 2025, **37**(4), 1–15, DOI: 10.15586/ijfs.v37i4.3033.

22 N. Bouzenad, N. Ammouchi, N. Chaib, Y. Belhocine, A. Belhaoues, N. Hamrouche, S. E. I. Boudagha, A. Abdennouri and W. Zahnit, Development of bioplastic films from Sargassum muticum alginate: Properties and applications in food packaging, *Iran. J. Chem. Chem. Eng.*, 2024, **43**(10), 3794–3811, DOI: 10.30492/ijcce.2024.2023449.6460.

23 S. Mouffok, E. Massutí, B. Zitouni, B. Guijarro, F. Ordines and K. Fliti, Ecology and fishery of the deep-water shrimp Aristeus antennatus (Risso, 1816) off Algeria (south-western Mediterranean), *Crustaceana*, 2008, **81**(10), 1177–1199, DOI: 10.1163/156854008X374513.

24 F. Fiorentino, G. Garofalo, G. Bono and S. Vitale, Learning from the history of red shrimp fisheries in the Mediterranean to improve sustainability of deep-water bottom trawling, *ICES J. Mar. Sci.*, 2024, **81**(3), 1–13, DOI: 10.1093/icesjms/fsae031.

25 N. Rossi and C. Delerue-Matos, Shrimp waste upcycling: Unveiling the potential of polysaccharides, proteins, carotenoids, and fatty acids with emphasis on extraction techniques and bioactive properties, *Mar. Drugs*, 2024, **22**, 153, DOI: 10.3390/md22040153.

26 M. L. Maia, C. Grosso, M. F. Barroso, A. Silva, C. Delerue-Matos and V. F. Domingues, Bioactive compounds of shrimp shell waste from Palaemon serratus and Palaemon varians from the Portuguese coast, *Antioxidants*, 2023, **12**(2), 435, DOI: 10.3390/antiox12020435.

27 J. Wang, Y. Tan, H. Yang, L. Zhan, G. Sun and L. Luo, On the adsorption characteristics and mechanism of methylene blue by ball mill modified biochar, *Sci. Rep.*, 2023, **13**(1), 21174, DOI: 10.1038/s41598-023-48133-1.

28 F. Ebrahimzadeh and A. Akbari, Investigation of the adsorption mechanisms, chemical resistance and mechanical strength of the synthesized chitosan/activated carbon composite in methylene blue removal, *Sci. Rep.*, 2025, **15**(1), 37820, DOI: 10.1038/s41598-025-37820-0.

29 L. Z. Lee and M. A. Ahmad Zaini, One-step $ZnCl_2/FeCl_3$ composites preparation of magnetic activated carbon for effective adsorption of rhodamine B dye, *Toxin Rev.*, 2022, **41**(1), 64–81, DOI: 10.1080/15569543.2020.1837172.

30 N. Hamrouche, C. Djilani, P. Magri, Y. Belhocine, F. Djazi, M. Kezzar and N. Bouzenad, A novel biosorbent from raw pomegranate peel modified with $SnCl_2/FeCl_2$ for the adsorption of crystal violet cationic dye: Response surface methodology process optimization, thermodynamic, kinetic, isotherm, and recyclability studies, *Biomass Convers. Biorefin.*, 2025, **15**(6), 9445–9461, DOI: 10.1007/s13399-024-05737-5.

31 M. Uğurlu, H. Osman, A. Vaizoğullar and A. J. Chaudhary, Fluoroquinolones antibiotics adsorption onto polymer coated magnetic nanoparticular activated carbon, *Int. J. Eng. Sci. Technol.*, 2021, **5**(2), 81–104, DOI: 10.29121/IJOEST.v5.i2.2021.172.

32 J. S. Weaver, J. Whiting, V. Tondare, C. Beauchamp, M. Peltz, J. Tarr, T. Q. Phan and M. A. Donmez, The effects of particle size distribution on the rheological properties of the powder and the mechanical properties of additively manufactured 17-4 PH stainless steel, *Addit. Manuf.*, 2021, **39**, 101851, DOI: 10.1016/j.addma.2021.101851.

33 S. S. Haramkar, G. N. Thombre, S. V. Jadhav and B. N. Thorat, The influence of particle size, shape and distribution on cake filtration mechanics—A short review, *C. R. Chim.*, 2021, **24**(2), 255–265, DOI: 10.5802/crchim.84.

34 H. Moghadam, M. Zakeri and A. Samimi, Mono-size distribution index (MSDI): A new criterion for the quantitative description of size distribution, Part, *Sci. Technol.*, 2017, **35**, 71–76, DOI: 10.22104/JPST.2019.3455.1144.

35 B. A. Mvala, T. S. Munonde, M. F. Bambo, K. P. Matabola and P. N. Nomngongo, Reusable waste-derived magnetic mesoporous activated carbon for efficient preconcentration and adsorptive removal of fluoroquinolones, *Chem. Eng. J. Adv.*, 2025, **23**, 100771, DOI: 10.1016/j.ceja.2025.100771.

36 G. M. Mohamed, W. E. Rashwan, T. El-Nabarawy and A.-N. A. El-Hendawy, Removal of basic dyes from aqueous solution onto H_2SO_4-modified rice husk, Egypt, *J. Chem.*, 2021, **64**(1), 143–155, DOI: 10.21608/EJCHEM.2020.39613.2807.

37 T. Zhao, G. Dai, H. Gu and R. Sun, Adsorption characteristics of lead ions by sorghum vinasse, *Pol. J. Environ. Stud.*, 2022, **31**(4), 3447–3454, DOI: 10.15244/pjoes/146008.

38 D. Damahe, N. Mayilswamy and B. Kandasubramanian, Biochar/metal nanoparticle-based composites for dye remediation: A review, *Hybrid Adv.*, 2024, **6**, 100254, DOI: 10.1016/j.hybadv.2024.100254.

39 A. Dbik, N. El Messaoudi, S. Bentahar, M. El Khomri, A. Lacherai and N. Faska, Optimization of methylene blue adsorption on agricultural solid waste using Box–Behnken design combined with response surface methodology modeling, *Biointerface Res. Appl. Chem.*, 2022, **12**(4), 4567–4583, DOI: 10.33263/BRIAC124.45674583.

40 N. Hamrouche, C. Djilani, Y. Belhocine, N. Bouzenad, L. Boudjema Amir, S. Meradi, I. Hamrouche and D. S. B. Ali, Comprehensive characterization and RSM-based optimization of crystal violet adsorption using $SnCl_2$–$FeCl_3$ and $SnCl_2$–$ZnCl_2$ activated pomegranate peel biosorbents, *RSC Adv.*, 2026, **16**(5), 4318–4334, DOI: 10.1039/D5RA09290F.

41 M. T. Moustafa, Preparation and characterization of low-cost adsorbents for the efficient removal of malachite green using response surface modeling and reusability studies, *Sci. Rep.*, 2023, **13**(1), 4493, DOI: 10.1038/s41598-023-31391-4.

42 M. T. M. H. Hamad, Optimization study of malachite green adsorption using MgO nanocomposite, nano-bentonite and fungal immobilization on activated carbon: Response surface methodology and kinetic study, *Environ. Sci. Eur.*, 2023, **35**(1), 26, DOI: 10.1186/s12302-023-00728-1.

43 W. Plazinski, W. Rudzinski and A. Plazinska, Theoretical models of sorption kinetics including a surface reaction mechanism: A review, *Adv. Colloid Interface Sci.*, 2009, **152**(1–2), 2–13, DOI: 10.1016/j.cis.2009.07.009.

44 H. Moussout, H. Ahlafi, M. Aazza and H. Maghat, Critical evaluation of linear and nonlinear equations of pseudo-first-order and pseudo-second-order kinetic models, *Karbala Int. J. Mod. Sci.*, 2018, **4**(2), 244–254, DOI: 10.1016/j.kijoms.2018.04.001.

45 A. Samanth, R. Selvaraj, G. Murugesan, T. Varadavenkatesan and R. Vinayagam, Efficient adsorptive removal of 2,4-dichlorophenoxyacetic acid (2,4-D) using biomass-derived magnetic activated carbon nanocomposite in synthetic and simulated agricultural runoff water, *Chemosphere*, 2024, **361**, 142513, DOI: 10.1016/j.chemosphere.2024.142513.

46 C. Djama, A. Bouguettoucha, D. Chebli, A. Amrane, H. Tahraoui, J. Zhang and L. Mouni, Experimental and theoretical study of methylene blue adsorption on a new raw material (Cynara scolymus): A statistical physics assessment, *Sustainability*, 2023, **15**, 10364, DOI: 10.3390/su151310364.

47 M. Challa and S. Chinnam, Non-linear kinetic, isotherm models approach for mercury adsorption on facile synthesized activated carbon from Zea mays roots, *Iran. J. Chem. Chem. Eng.*, 2024, **43**(1), 119–131, DOI: 10.30492/ijcce.2023.1989826.5877.

48 N. Onursal, Application of a new adsorption kinetic model for the removal of Zn(II) ions from aqueous solutions using Malatya clay, *J. King Saud Univ., Sci.*, 2025, **37**(1), 103333, DOI: 10.1016/j.jksus.2024.103333.

49 A. A. Sangoremi, Adsorption kinetic models and their applications: A critical review, *Int. J. Res. Sci. Innov.*, 2025, **12**(5), 245–258, DOI: 10.51244/IJRSI.2025.120500019.

50 A. Acharya, G. Jeppu, C. R. Girish, B. Prabhu, V. R. Murty, A. S. Martis and S. Ramesh, Adsorption of arsenic and fluoride: Modeling of single and competitive adsorption systems, *Heliyon*, 2024, **10**(11), e31967, DOI: 10.1016/j.heliyon.2024.e31967.

51 A. O. Dada, A. P. Olalekan, A. M. Olatunya and O. Dada, Langmuir, Freundlich, Temkin and Dubinin–

Radushkevich isotherm studies of equilibrium sorption of Zn^{2+} onto phosphoric acid-modified rice husk, *IOSR J. Appl. Chem.*, 2012, **3**(1), 38–45, DOI: 10.9790/5736-0313845.

52 A. Benmessaoud, D. Nibou, E. H. Mekatel and S. Amokrane, A comparative study of linear and non-linear methods for determining the optimum equilibrium isotherm for adsorption of Pb^{2+} ions onto Algerian treated clay, Iran, *J. Chem. Chem. Eng.*, 2020, **39**(4), 153–171, DOI: 10.30492/ijcce.2019.35116.

53 R. Ragadhita and A. B. D. Nandiyanto, How to calculate adsorption isotherms of particles using two-parameter monolayer adsorption models and equations, *Indones. J. Sci. Technol.*, 2021, **6**(1), 205–234, DOI: 10.17509/ijost.v6i1.32354.

54 B. T. Danat, R. A. Wuana, H. F. Chahul and M. S. Iorungwa, Review of adsorption isotherms models, *Appl. Water Sci.*, 2026, **16**(3), 72, DOI: 10.1007/s13201-025-02682-0.

55 A. Saleem, R. Hassan, M. Ehtisham, M. S. Almatawa, A. K. Badawi and B. Ismail, Influence of nickel doping on the moisture adsorption properties of magnesium aluminate spinel: Thermodynamic and kinetic analysis, *RSC Adv.*, 2026, **16**(11), 9399–9411, DOI: 10.1039/D5RA09380E.

56 A. B. D. Nandiyanto, N. N. Azizah and S. Rahmadianti, Isotherm study of banana stem waste adsorbents for reducing textile dyeing wastewater concentration, *J. Engine Res.*, 2021, 16063, DOI: 10.36909/jer.ASSEEE.16063.

57 E. Öztürk Er, S. Gürsoy and S. Bakırdere, Equilibrium modelling and kinetic studies on adsorption of cadmium from lake water by a magnetic covalent organic framework, *Sci. Rep.*, 2026, **16**, 4838, DOI: 10.1038/s41598-025-34851-1.

58 İ. Küçük, Methylene blue adsorption capacity and coherent isotherm model of commercial activated carbon, *Cumhuriyet Sci. J.*, 2021, **42**(4), 843–851, DOI: 10.17776/csj.861860.

59 P. Ramadhani, Z. Chaidir, Zilfa, Z. B. Tomi, D. Rahmiarti and R. Zein, Shrimp shell (Metapenaeus monoceros) waste as a low-cost adsorbent for metanil yellow dye removal from aqueous solution, *Desalin. Water Treat.*, 2020, **197**, 413–423, DOI: 10.5004/dwt.2020.25963.

60 O. P. Gbenebor, S. O. Adeosun, G. I. Lawal and S. Jun, Role of $CaCO_3$ in the physicochemical properties of crustacean-sourced structural polysaccharides, *Mater. Chem. Phys.*, 2016, **184**, 203–209, DOI: 10.1016/j.matchemphys.2016.09.043.

61 E. Misran, W. Pratama, K. I. K. Napitupulu, M. D. Supardan, D. A. Iryani and V. Pramananda, Ultrasonic-assisted adsorption of methylene blue using shrimp shells as a low-cost adsorbent: Evaluation of adsorption isotherm, kinetics, and thermodynamics, *S. Afr. J. Chem. Eng.*, 2025, **52**, 111–126, DOI: 10.1016/j.sajce.2025.01.011.

62 N. Mennas, S. Lahreche, F. Chouli, L. Sabantina and A. Benyoucef, Adsorption of methylene blue dye by cetyltrimethylammonium bromide intercalated polyaniline-functionalized montmorillonite clay nanocomposite: Kinetics, isotherms, and mechanism study, *Polymers*, 2023, **15**(17), 3518, DOI: 10.3390/polym15173518.

63 H. Yu, Y. Zhang, L. Wang, Y. Tuo, S. Yan, J. Ma, X. Zhang, Y. Shen, H. Guo and L. Han, Experimental and DFT insights into the adsorption mechanism of methylene blue by alkali-modified corn straw biochar, *RSC Adv.*, 2024, **14**(3), 1854–1865, DOI: 10.1039/D3RA07049A.

64 C. Djilani, R. Zaghdoudi, F. Djazi, A. Lallam, B. Bouchekima and P. Magri, Comparative study of photocatalytic activity of nanocomposites prepared from biological wastes and ZnO nanoparticles, *Desalin. Water Treat.*, 2021, **220**, 329–341, DOI: 10.5004/dwt.2021.27000.

65 S. Ngasotter, K. A. M. Xavier, L. Porayil, A. Balange, B. B. Nayak, S. Eapen, K. J. Adarsh, M. S. Sreekala, R. Sharma and G. Ninan, Optimized high-yield synthesis of chitin nanocrystals from shrimp shell chitin by steam explosion, *Carbohydr. Polym.*, 2023, **316**, 121040, DOI: 10.1016/j.carbpol.2023.121040.

66 S. Jana and V. K. Subramanian, Chelant–carbonate–sulfite combination program for scale inhibition: An atomistic-to-holistic approach and application, *Results Surf. Interfaces*, 2025, **18**, 100428, DOI: 10.1016/j.rsurfi.2025.100428.

67 A. A. Qureshi, S. Javed, H. M. A. Javed, M. Jamshaid, U. Ali and M. A. Akram, Systematic investigation of structural, morphological, thermal, optoelectronic, and magnetic properties of high-purity hematite/magnetite nanoparticles for optoelectronics, *Nanomaterials*, 2022, **12**(10), 1635, DOI: 10.3390/nano12101635.

68 Y. Zhou, L. Ge, N. Fan and M. Xia, Adsorption of Congo red from aqueous solution onto shrimp shell powder, *Adsorpt. Sci. Technol.*, 2018, **36**(5–6), 1310–1330, DOI: 10.1177/0263617418768945.

69 O. A. Salawu, Z. Han and A. S. Adeleye, Shrimp waste-derived porous carbon adsorbent: Performance, mechanism, and application of machine learning, *J. Hazard. Mater.*, 2022, **437**, 129266, DOI: 10.1016/j.jhazmat.2022.129266.

70 P. Ramadhani, Z. Chaidir, Zilfa, Z. B. Tomi, D. Rahmiarti and R. Zein, Shrimp shell (Metapenaeus monoceros) waste as a low-cost adsorbent for metanil yellow dye removal from aqueous solution, *Desalin. Water Treat.*, 2020, **197**, 413–423, DOI: 10.5004/dwt.2020.25963.

71 S. Brunauer, P. H. Emmett and E. Teller, Adsorption of gases in multimolecular layers, *J. Am. Chem. Soc.*, 1938, **60**, 309–319, DOI: 10.1021/ja01269a023.

72 S. K. S. W. Sing, D. H. Everett, R. A. W. Haul, L. Moscou, R. A. Pierotti, J. Rouquerol and T. Siemieniewska, Reporting physisorption data for gas/solid systems with special reference to the determination of surface area and porosity, *Pure Appl. Chem.*, 1985, **57**(4), 603–619, DOI: 10.1351/pac198557040603.

73 F. Ambroz, T. J. Macdonald, V. Martis and I. P. Parkin, Evaluation of the BET theory for the characterization of meso- and microporous MOFs, *Small Methods*, 2018, **2**(11), 1800173, DOI: 10.1002/smtd.201800173.

74 V. M. Gun'ko, Features of BET method application to various adsorbents, *Khim., Fiz. Tekhnol. Poverkhni*, 2022, **13**(3), 249–258, DOI: 10.15407/hftp13.03.249.
75 M. Thommes, K. Kaneko, A. V. Neimark, J. P. Olivier, F. Rodríguez-Reinoso, J. Rouquerol and K. S. W. Sing, Physisorption of gases, with special reference to the evaluation of surface area and pore size distribution (IUPAC technical report), *Pure Appl. Chem.*, 2015, **87**(9–10), 1051–1069, DOI: 10.1515/pac-2014-1117.
76 E. P. Barrett, L. G. Joyner and P. P. Halenda, The determination of pore volume and area distributions in porous substances. I. Computations from nitrogen isotherms, *J. Am. Chem. Soc.*, 1951, **73**(1), 373–380, DOI: 10.1021/ja01145a126.
77 G. L. Dotto, J. M. N. Santos, I. L. Rodrigues, R. Rosa, F. A. Pavan and E. C. Lima, Adsorption of methylene blue by ultrasonic surface modified chitin, *J. Colloid Interface Sci.*, 2015, **446**, 133–140, DOI: 10.1016/j.jcis.2014.12.050.
78 M. Vakili, M. Rafatullah, B. Salamatinia, A. Z. Abdullah, M. H. Ibrahim, K. B. Tan, Z. Gholami and P. Amouzgar, Application of chitosan and its derivatives as adsorbents for dye removal from water and wastewater: A review, *Carbohydr. Polym.*, 2014, **113**, 115–130, DOI: 10.1016/j.carbpol.2014.07.007.
79 A. Elkhaleefa, I. H. Ali, E. I. Brima, I. Shigidi, A. B. Elhag and B. Karama, Evaluation of adsorption efficiency for the removal of Pb(II) ions from aqueous solutions using Azadirachta indica leaves as an adsorbent, *Processes*, 2021, **9**, 559, DOI: 10.3390/pr9030559.
80 T. Zhong, M. Xia, Z. Yao and C. Han, Chitosan/silica nanocomposite preparation from shrimp shell and its adsorption performance for methylene blue, *Sustainability*, 2022, **15**(1), 47, DOI: 10.3390/su15010047.
81 J. B. Adeoye, S. Y. Lau, Y. H. Tan, Y. Y. Tan, T. Chiong, N. M. Mubarak, G. Anbuchezhiyan, M. Khalid and J. T. W. Ng, A comprehensive review on adsorption technologies for methylene blue elimination: Efficiency, mechanisms, and future perspectives, *Discover Appl. Sci.*, 2025, **7**(11), 1285, DOI: 10.1007/s42452-025-07250-4.
82 M. A. Ludeña, F. de L. Meza, R. I. Huamán, A. M. Lechuga and A. C. Valderrama, Preparation and characterization of Fe_3O_4/poly(HEMA-co-IA) magnetic hydrogels for removal of methylene blue from aqueous solution, *Gels*, 2023, **10**(1), 15, DOI: 10.3390/gels10010015.
83 A. Saad, A. A. Galhoum, N. Hamad and S. Wageh, Phosphorylated chitosan nanosorbents from shrimp waste for enhanced dual removal of methylene blue and lead (II), *J. Environ. Chem. Eng.*, 2025, **13**, 119766, DOI: 10.1016/j.jece.2025.119766.
84 B. A. Al-Mur and M. T. Jamal, Eco-friendly dye removal using chitosan: Characterization and kinetic modeling of methylene blue and methyl orange adsorption, *Polymers*, 2026, **18**(5), 546, DOI: 10.3390/polym18050546.
85 U. H. Alozie, C. B. Mba, M. C. Sunday, U. F. Onwuka, L. J. King, M. C. Anukwonke and O. G. Uzokwe, Adsorption of methylene blue from aqueous solutions using activated carbon derived from sand box seed shell (*Hura crepitans*): Isothermal, thermodynamic, and kinetic studies, *J. King Saud Univ., Eng. Sci.*, 2026, **38**(1), 4, DOI: 10.1007/s44444-025-00090-y.
86 K. Duodu, G. W. Ashong, F. Opoku, N. O. Boadi and E. S. Agorku, Equilibrium, kinetic and thermodynamic studies of the adsorption of Congo red on nZVI/Zn–Al layered double hydroxide intercalated with PO_4^{3-} ion, *Discov. Sustain.*, 2025, **6**(1), 449, DOI: 10.1007/s43621-025-00979-3.
87 A. Maghsoudi and A. Khajeh-Amiri, Magnetically activated carbon fibers felt (MACFF) as an effective adsorbent for successful removal of cephalexin and amoxicillin from water, *Results Chem.*, 2025, **13**, 102030, DOI: 10.1016/j.rechem.2025.102030.
88 A. El-Rayyes, I. Arogundade, E. A. Ofudje, M. S. Refat, A. M. Alsuhaibani, J. A. Akande and E. F. Sodiya, Thermodynamic, isotherm and kinetic studies lead ions adsorption onto *Manihot esculenta* chaff surface, *Sci. Rep.*, 2025, **15**(1), 27672, DOI: 10.1038/s41598-025-27672-0.
89 M. Uğurlu, H. Osman, A. İ. Vaizoğulları and A. J. Chaudhary, Adsorptive removal of oxytetracycline using polymer-coated magnetic nanoparticulate activated carbon: Synthesis, characterization, adsorption isotherms and kinetics studies, *Iran. J. Chem. Chem. Eng.*, 2022, **41**(9), 2986–3006, DOI: 10.30492/ijcce.2021.525693.4593.
90 C. R. Girish, Determination of thermodynamic parameters in adsorption studies: A review, *Chem. Pap.*, 2025, **79**, 5687–5706, DOI: 10.1007/s11696-025-04218-x.
91 C. N. Adewumi, E. D. Agbaghare and E. J. Emmanuel, Kinetics–thermodynamics integration for improved understanding of adsorption mechanisms: A critical perspective, *World J. Adv. Res. Rev.*, 2025, **27**(2), 417–443, DOI: 10.30574/wjarr.2025.27.2.283.
92 H. M. El Refay, A. Goma, N. Badawy and F. A. Z. Ghanem, Agricultural by-products as green adsorbents for elimination of Reactive Red 43 from aqueous media: Adsorption properties and thermodynamic study, Egypt, *J. Chem.*, 2022, **65**(8), 97–108, DOI: 10.21608/ejchem.2022.102614.4757.
93 N. M. Aljamali, R. Khdur and I. O. Alfatlawi, Physical and chemical adsorption and its applications, *Int. J. Thermodyn. Chem. Kinet.*, 2021, **7**(2), 1–8, DOI: 10.37628/IJTCK.
94 V. J. Inglezakis and A. A. Zorpas, Heat of adsorption, adsorption energy and activation energy in adsorption and ion exchange systems, *Desalin. Water Treat.*, 2012, **39**(1–3), 149–157, DOI: 10.1080/19443994.2012.669169.
95 R. A. Kausar, Methylene blue adsorption isotherm on *Spirulina sp.* microalgae biomass coated by silica-magnetite, *IOP Conf. Ser.:Mater. Sci. Eng.*, 2020, **857**, 012019, DOI: 10.1088/1757-899X/857/1/012019.
96 M. Reji and R. Kumar, Response surface methodology (RSM): An overview for multivariate data analysis, *Indian J. Microbiol. Res.*, 2022, **9**, 241–248, DOI: 10.18231/j.ijmr.2022.042.
97 Y. Depari, A. A. Tanjung and A. A. Kacaribu, Broccoli waste protein hydrolysate–modified chitosan with iron sand for

methylene blue adsorption from water, *Results Chem.*, 2026, 103164, DOI: 10.1016/j.rechem.2026.103164.

98 I. Y. Erwa, O. Ishag, O. Alrefaei and I. Hassan, Nonlinear fitting for estimation of adsorption equilibrium, kinetic and thermodynamic parameters of methylene blue onto activated carbon, *J. Turk. Chem. Soc., Sect. A*, 2022, **9**(1), 67–84, DOI: 10.18596/jotcsa.904311.

99 E. O. Al-Saigh, A. F. Al-Omari and R. H. Al-Hyali, Chitosan/sunflower seed husk composite hydrogel for the removal of methylene blue from wastewater, *Res. J. Chem. Environ.*, 2025, **29**(11), 01, DOI: 11.1554/Rjce.11.11.2025.01.

100 T. Zhong, M. Xia, Z. Yao and C. Han, Chitosan/silica nanocomposite prepared from shrimp shell and its adsorption performance for methylene blue, *Sustainability*, 2023, **15**(1), 47, DOI: 10.3390/su15010047.

101 L. Zeng, M. Xie, Q. Zhang, Y. Kang, X. Guo, H. Xiao, Y. Peng and J. Luo, Chitosan/organic rectorite composite for the magnetic uptake of methylene blue and methyl orange, *Carbohydr. Polym.*, 2015, **123**, 89–98, DOI: 10.1016/j.carbpol.2015.01.045.

102 A. S. A. Khalaf-Allah, M. Sultan, Y. K. Abdel-Monem, S. M. El-Gamasy, W. A. El-Sayed and A. M. Youssef, Boosting adsorption capacity of methylene blue dye using multifunctional ZnO-g-C_3N_4/carboxymethyl chitosan/alginate-grafted poly(acrylic acid) composite, *Sci. Rep.*, 2025, **15**, 43482, DOI: 10.1038/s41598-025-29715-7.

103 R. Zein, S. Wulandari, P. Ramadhani and D. Deswati, Utilization of shrimp shell as a low-cost biosorbent for methylene blue dye adsorption, *Ecol. Chem. Eng. S*, 2024, **31**(1), 63–73, DOI: 10.2478/eces-2024-0005.

104 E. Igberase and I. G. Mkhize, Efficient adsorption of methylene blue (MB) by an eco-friendly chitosan derivative adsorbent: An RSM and ANN modeling study, *Desalin. Water Treat.*, 2025, **321**, 100943, DOI: 10.1016/j.dwt.2025.100943.

105 R. A. Kausar, Buhani and Suharso, Methylene blue adsorption isotherm onto Spirulina sp. microalgae biomass coated with silica–magnetite, *IOP Conf. Ser.:Mater. Sci. Eng.*, 2020, **857**, 012019, DOI: 10.1088/1757-899X/857/1/012019.

106 A. Y. Ahmed, A. K. Kareem, H. AlMohamadi, M. Y. H. Al-Shamri, F. F. Sead, N. Juraev, A. Saad, Z. I. Al-Mashhadani, C.-Y. Hsu and B. S. Shaheen, Fabrication and characterization of a novel magnetic nanocomposite based on chitosan hydrogel modified with mesoporous silica and copper-based MOF as an effective and antibacterial adsorbent for the removal of methylene blue from water, *Int. J. Biol. Macromol.*, 2025, 148643, DOI: 10.1016/j.ijbiomac.2025.148643.

107 A. C. Blaga, R. Cimpoesu, R.-E. Tataru-Farmus and D. Suteu, Eco-friendly biosorbents from biopolymers and food waste for efficient dye removal from wastewater, *Polymers*, 2025, **17**(3), 291, DOI: 10.3390/polym17030291.